Experimental Implementation of a Four-Level N-type Scheme for the Observation of Electromagnetically Induced Transparency

V. M. Éntin*, I. I. Ryabtsev, A. E. Boguslavskiĭ, and I. M. Beterov[†]

Institute of Semiconductor Physics, Siberian Division, Russian Academy of Sciences,
pr. Akademika Lavrent'eva 13, Novosibirsk, 630090 Russia
*e-mail: ventin@isp.nsc.ru

Received January 31, 2000

Abstract—A nondegenerate four-level N-type scheme was experimentally implemented to observe electromagnetically induced transparency (EIT) at the ^{87}Rb D_2 line. Radiations of two independent external-cavity semiconductor lasers were used in the experiment, the current of one of them being modulated at a frequency equal to the hyperfine-splitting frequency of the excited $5P_{3/2}$ level. In this case, apart from the main EIT dip corresponding to the two-photon Raman resonance in a three-level Λ-scheme, additional dips detuned from the main dip by a frequency equal to the frequency of the HF generator were observed in the absorption spectrum. These dips were due to an increase in the medium transparency at frequencies corresponding to the three-photon Raman resonances in four-level N-type schemes. The resonance shapes are analyzed as functions of generator frequency and magnetic field.© *2000 MAIK "Nauka/Interperiodica".*

PACS numbers: 32.80.Qk; 42.50.Gy

The nonlinear interference effect [1] underlies numerous studies on coherent population trapping [2, 3], inversionless amplification [4], electromagnetically induced transparency [5], atomic laser cooling and capture [6], phase control of atomic states [7], etc. Initiation of electromagnetically induced transparency (EIT) in a medium with coherent pumping is one of the most prominent interference phenomena and manifests itself as narrow dips in the absorption spectra of atoms interacting with multifrequency resonance radiation.

As a rule, the experiments on EIT of alkali-metal atoms are carried out using the Λ-scheme of transitions in the laser radiation field modulated at a frequency equal to the ground-state hyperfine- or Zeeman-splitting frequency [8] or in the field of two phase-locked lasers [9]. The scanning of modulation frequency (or frequency difference in the case of two lasers) gives rise to a narrow interference resonance at the point corresponding to the exact two-photon Raman resonance between two ground-state sublevels coupled to the same excited state.

The use of the four-level N-type schemes of resonance transitions, for which Zeeman coherence can be spontaneously transferred from the excited to the ground level [10], opens up new opportunities for studying nonlinear phenomena. Such a scheme was investigated both theoretically [11] and experimentally [8, 12] for the quasidegenerate upper and lower states

[†] Deceased.

interacting with a two-frequency laser emission in a weak magnetic field. It was shown that the coherence transfer can give rise not only to the EIT but also to the electromagnetically induced absorption.

This paper reports the results of experimental implementation of the nondegenerate four-level N-type scheme for the observation of the EIT in a three-frequency laser radiation field. The experiments were carried out using the radiations of two independent semiconductor lasers, one of which was modulated at a frequency equal to the hyperfine-splitting frequency of the excited $5P_{3/2}$ state of the ^{87}Rb atom. Therefore, the three-photon Raman resonance N-type scheme has been implemented for initiating EIT.

Experiments were carried out on the optical transitions between the hyperfine-structure components of the ^{87}Rb D_2 absorption line (the $5S_{1/2} \longrightarrow 5P_{3/2}$ transition at a wavelength of 780 nm). The experimental setup is schematically shown in Fig. 1a. Two HL7851MG diode lasers with external cavities were used as radiation sources. The generation linewidth did not exceed 1 MHz. For tuning to different transitions, a portion of the radiation was diverted into two independent saturated-absorption sections *1* and *2* (according to [13]). The remaining portion of the radiation was combined in a collinear geometry. The wave fronts were carefully brought into coincidence by means of a set of mirrors and diaphragm *3*. The polarization plane of one of the radiations was turned through 90° by a
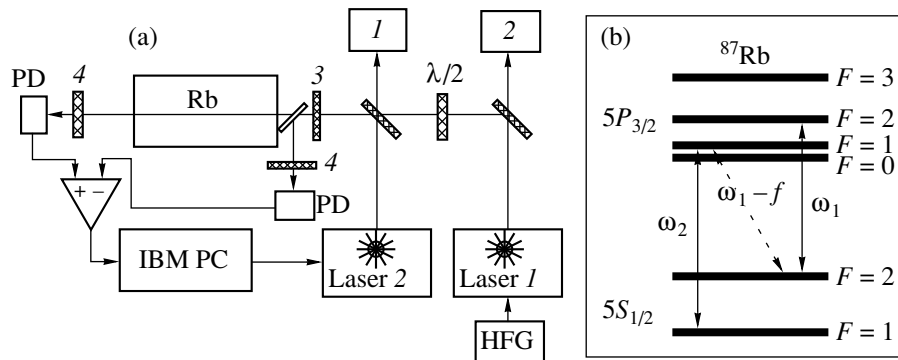
Fig. 1. (a) Experimental setup. (*1* and *2*, schemes of saturated absorption spectroscopy; *3*, diaphragm; *4*, polaroids; PD, photodiodes; HFG, high-frequency generator). (b) Scheme of the ^{87}Rb D_2 line transitions occurring in the presence of HF modulation of laser *1*.

half-wave plate for further detection of the separate absorption signals of the two beams using polaroids *4*. The beams passed through the absorption cell containing the ^{87}Rb isotope vapor at temperatures from 20 to 40°C. The laser beam intensities were as high as 20 and 30 mW/cm^2 for lasers *1* and *2*, respectively.

High-frequency modulation of the current of laser *1* was accomplished by an HF generator. Its frequency f was varied near 156.9 MHz, i.e., near the frequency difference between the hyperfine-structure sublevels $F = 1$ and 2 of the excited $5P_{3/2}$ state (Fig. 1b). Switching on the generator resulted in the appearance of side frequencies shifted by $\pm f$ from the center frequency of the
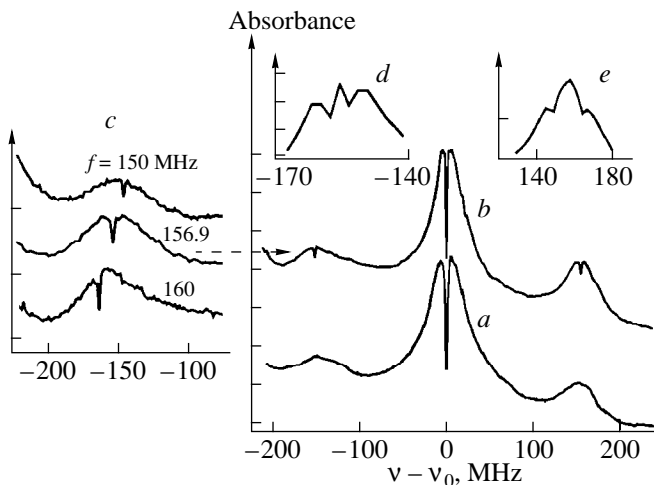

Fig. 2. (*a*) Absorption of the radiation of laser *1* recorded upon scanning the frequency of laser *2*. (*b*) The same spectrum with the switched-on HF modulation of laser *1*. (*c*) Positions of additional resonances at different frequencies of HF generator. (*d*) Shape of the additional resonance $5S_{1/2} (F = 1) \longleftrightarrow 5P_{3/2} (F = 1) \longleftrightarrow 5S_{1/2} (F = 2) \longleftrightarrow 5P_{3/2} (F = 2)$ (left in Fig. 2b) in a transverse magnetic field of 10 G. (*e*) The same for the $5S_{1/2} (F = 1) \longleftrightarrow 5P_{3/2} (F = 2) \longleftrightarrow 5S_{1/2} (F = 2) \longleftrightarrow 5P_{3/2} (F = 1)$ resonance (right in Fig. 2b).

emission spectrum of laser *1*. Their intensities were one-tenth that of the center frequency.

The direction and strength of the constant magnetic field in the cell were defined by three pairs of Helmholtz coils. This made it possible to compensate the laboratory magnetic field, which was equal to 0.7 G and considerably affected the resonance amplitudes.

Absorption of the radiation from laser *1* was recorded simultaneously by tuning the frequency ω_2 of laser *2* within the Doppler profile of a group of the $5S_{1/2}(F = 1) \longrightarrow 5P_{3/2}(F = 0, 1, 2)$ transitions (Fig. 1b), Doppler broadening of individual resonances was 520 MHz. In this case, the center frequency ω_1 of laser *1* was fixed and tuned to the center of the Doppler profile of a group of the $5S_{1/2}(F = 2) \longrightarrow 5P_{3/2}(F = 1, 2, 3)$ transitions. The frequency of laser *2* was computer-controlled.

The absorption signal ω_1 represented the sum of signals from three groups of atoms with different velocity projections. Due to the Doppler effect, each of them was in resonance with one of the three transitions. In the absence of emission ω_2, the absorption at frequency ω_1 was at a certain fixed level (about 10%) determined by the atomic concentration, saturation parameters, relaxation rates, etc.

After switching on and scanning frequency ω_2, several peaks with different amplitudes appeared in the absorption spectrum ω_1 (Fig. 2a). The increase in the absorption at certain values of frequency ω_2 was caused by an increase in the population of the $5S_{1/2} (F = 2)$ level due to the spontaneous decay of the $5P_{3/2} (F = 1, 2)$ levels excited by radiation ω_2. The peak widths (ca. 40 MHz) were mostly due to the power broadening of the resonances and decreased with decreasing laser radiation intensity. The frequency spacings between the peaks were equal to the hyperfine-splitting frequencies of the excited $5P_{3/2}$ state.

In the absence of HF modulation of laser *1*, only one of the peaks had the interference EIT dip at its center (Fig. 2a). The dip corresponded to the summarized signal from the two-photon Raman resonances $5S_{1/2} (F = 1) \longleftrightarrow 5P_{3/2} (F = 1) \longleftrightarrow 5S_{1/2} (F = 2)$ and

$5S_{1/2}$ ($F = 1$) $\longleftrightarrow$ $5P_{3/2}$ ($F = 2$) $\longleftrightarrow$ $5S_{1/2}$ ($F = 2$) in two groups of atoms with different velocity projections. The dip width fell in the range 2.6–4 MHz and was less than the natural linewidth (6 MHz). It is known that the width of EIT resonances depends strongly on the fluctuations of the phase and frequency differences of laser radiations and can be tangibly reduced upon matching the phases of two radiations if the depolarizing collisions are absent [10]. In our case, two independent lasers and a cell with rubidium vapor at low pressure without buffer gas were used, so that the width of the interference resonances was mainly determined by the width of the laser spectra.

The EIT resonance was most contrasting in the case of orthogonal linear polarizations of radiations ω_1 and ω_2. To enhance contrast, it was necessary to compensate the laboratory magnetic field.

Switching on the HF modulation of laser 1 resulted in the appearance of the additional EIT dips at the tops of the two neighboring absorption peaks detuned by the $F = 1, 2$ interval of the hyperfine structure of the $5P_{3/2}$ state (Fig. 2b). Because of the presence of side frequencies in the spectrum of laser 1, these dips were due to the three-photon Raman resonances $5S_{1/2}$ ($F = 1$) $\longleftrightarrow$ $5P_{3/2}$ ($F = 1$) $\longleftrightarrow$ $5S_{1/2}$ ($F = 2$) $\longleftrightarrow$ $5P_{3/2}$ ($F = 2$) (left dip in Fig. 2b) and $5S_{1/2}$ ($F = 1$) $\longleftrightarrow$ $5P_{3/2}$ ($F = 2$) $\longleftrightarrow$ $5S_{1/2}$ ($F = 2$) $\longleftrightarrow$ $5P_{3/2}$ ($F = 1$) (right dip in Fig. 2b) in two groups of atoms with different velocity projections. The frequency detuning of the additional dips from the main EIP resonance was equal to the HF-generator frequency. As the frequency varied over the range 156.9 ± 15 MHz, the dips changed their positions at the tops of the peaks (Fig. 2c) and disappeared at large detuning.

Note that, at the exact resonance, the radiations at three frequencies, ω_1, ω_2, and ($\omega_1 + f$) or ($\omega_1 - f$), interact simultaneously with each atomic group. This interaction generates a coherent superposition of atomic state, for which the absorption of laser radiations decreases (dark resonance). The appearance of the dark resonance underlies the phenomenon of electromagnetically induced transparency.

The additional EIT dips were most contrasting in the presence of a weak (≤ 0.5 G) longitudinal (collinear with the direction of the laser beams) magnetic field but disappeared at a field strength above 2.5 G. At the same time, the indicated fields had almost no effect on the shape and amplitude of the main EIT resonance.

In the case of a transverse magnetic field, the resonances did not disappear, allowing their Zeeman splitting to be observed. Figures 2d and 2e show the experimental records of the additional dips in the presence of a 10-G magnetic field aligned with the polarization vector of the ω_1 wave. A sizably different behavior of the resonances in Figs. 2d and 2e is noteworthy. Despite the low contrast, the resonance structure shown in Fig. 2e allows one to assume that an inverted dip is present at the center and that its origin is the same as the origin of the inverted dips observed in [8, 11, 12]; i.e., it is the

electromagnetically induced absorption. However, an analysis of the rather complex shape of the resonances observed in our case requires careful theoretical consideration and numerical calculations with taking into account the Zeeman splitting of atomic levels.

The effect demonstrated in this work is the implementation of the nondegenerate four-level N-type scheme for initiating the EIT in the field of three-frequency laser radiation. At the same time, it can be treated as a frequency shift of the EIT resonances under the HF modulation of the laser radiation. This effect can be applied in a wide variety of problems in the field of nonlinear laser spectroscopy, in particular, in various schemes of laser cooling and in the experiments on inversionless amplification and lasing. Note in conclusion that the observed resonances can have extremely small widths if the magnetic field is accurately compensated and the laser radiations are closely phase-locked.

REFERENCES

1. T. Ya. Popova, A. K. Popov, S. G. Rautian, and R. I. Sokolovskiĭ, Zh. Éksp. Teor. Fiz. **57**, 850 (1969) [Sov. Phys. JETP **30**, 466 (1969)].

2. G. Alzetta, A. Gozzini, L. Moi, and G. Orriols, Nuovo Cimento B **36**, 5 (1976).

3. E. Arimondo, in *Progress in Optics*, Ed. by E. Wolf (North-Holland, Amsterdam, 1996), Vol. 35, p. 257.

4. A. S. Zibrov, M. D. Lukin, D. E. Nikonov, *et al.*, Phys. Rev. Lett. **75**, 1499 (1995).

5. D. J. Fulton, S. Shepherd, R. R. Mosely, *et al.*, Phys. Rev. A **52**, 2302 (1995).

6. C. N. Cohen-Tannoudji, Rev. Mod. Phys. **70**, 707 (1998).

7. M. Shapiro and P. Brumer, Trans. Faraday Soc. **82**, 177 (1997).

8. A. M. Akulshin, S. Barreiro, and A. Lezama, Phys. Rev. A **57**, 2996 (1998).

9. R. Wynands and A. Nagel, Appl. Phys. B **68**, 1 (1999).

10. S. G. Rautian, Pis'ma Zh. Éksp. Teor. Fiz. **61**, 461 (1995) [JETP Lett. **61**, 473 (1995)].

11. A. V. Taĭchenachev, A. M. Tumaĭkin, and V. I. Yudin, Pis'ma Zh. Éksp. Teor. Fiz. **69**, 776 (1999) [JETP Lett. **69**, 819 (1999)].

12. A. Lezama, S. Barreiro, and A. M. Akulshin, Phys. Rev. A **59**, 4732 (1999).

13. K. B. MacAdam, A. Steinbach, and C. Wieman, Am. J. Phys. **60**, 1098 (1992).

Translated by R. Tyapaev

===== **PLASMA, GASES** =====

Dynamically Stable Electron Bunches in Beam Interaction with an Electromagnetic Wave Packet[1]

A. S. Volokitin* and C. Krafft**

* *Institute of Terrestrial Magnetism, the Ionosphere, and Radiowave Propagation, Russian Academy of Sciences, Troitsk, Moscow oblast, 142092 Russia*
** *Laboratoire de Physique des Gaz et des Plasmas, Université Paris Sud, 91405 Orsay Cedex, France*
Received January 28, 2000

Abstract—Nonlinear interaction of electron beam with a whistler wave packet that effectively dissipates through collisions or wave leakage is studied. Independently of the dissipation type and nature of waves, self-organization of the beam structure leads to the formation of bunches continuously decelerated by waves. Strong dissipation prevents phase mixing required for the quasilinear theory and keeps wave phases in the packet correlated. Thus, dynamically stable bunches are present together with a plateau in the velocity distribution; asymptotically, wave emission by bunches is the main process. © 2000 MAIK "Nauka/Interperiodica".

PACS numbers: 41.60.Bq; 41.75.Fr; 52.35.Hr; 52.40.Mj

The study of energetic beam interaction with electromagnetic waves in magnetized plasmas is motivated by many laboratory and space experiments involving beam injection [1–9] and by observations of natural suprathermal particle fluxes traveling in planetary, solar, and astrophysical plasmas [10–12]. For example, emission of extremely low-frequency waves by modulated and pulsed electron beams injected by satellites into the Earth's ionosphere and magnetosphere have been observed in several active space experiments [4–9].

In particular, theoretical investigations of the nonlinear dynamics of electron beam resonant interaction with whistler waves were mainly devoted to the case of a single monochromatic wave or to the quasilinear theory of boundless beam relaxation in plasma with a continuous wave spectrum [13–15]. It was particularly shown [16–19] that, in the presence of strong dissipation, the nonlinear interaction of a monoenergetic electron beam with a single wave differs considerably from the nondissipative case: the beam–wave system exhibits a strong tendency to self-organization. Indeed, the dissipative effects due to the collisions in plasma or to the effective wave radiation out of the bounded volume of a thin beam make the system nonconservative and, as a result of the irreversible loss of wave momentum and energy, prevent the periodic energy exchange between the beam and the wave. At the same time, the nonlinear evolution of resonant particles is characterized by the formation of dynamically stable electron bunches that are continuously decelerated and supply energy to the wave through the resonant Cherenkov interaction caused by a self-adjusted nonlinear shift of the parallel wave number [16–18].

In this letter, we report and explain, for the first time, physical effects of this type occurring during the nonlinear interaction of an electron beam with a packet of whistlers; moreover, it is shown that different types of dissipative beam–wave interaction can be described by similar mechanisms. In the case of a wave packet, the bunched particles exchange energy with several waves, so that one could expect that the beam–wave system should evolve according to the quasilinear theory (diffusion to lower velocities and plateau formation). However, in the presence of strong losses of wave energy, the phases of all waves can become strongly correlated and thus prevent the stochastic phase mixing required for the validity of the quasilinear theory. This letter presents a theoretical model and relevant numerical simulations explaining the nonlinear evolution of the beam–wave system in terms of dynamic energy exchange, particle trapping, slowing down of the beam, self-organization of complex bunched electron structures, and quasilinear diffusion.

As an interesting practical example of a dissipative system, we consider here a nonlinear model developed to study whistler emission through the Cherenkov resonance of a density-modulated thin electron beam. A beam of small radius r_b and cylindrical symmetry is injected along the ambient magnetic field $\mathbf{B}_0 = B_0 \mathbf{z}$ with a fixed modulation frequency. The evolution of a beam-current modulation is considered self-consistently as the result of a nonlinear motion of beam particles in the whistler fields. Wave fields outside the beam are described in the approximation of a fixed beam radius, because $\mathbf{B}_0$ stabilizes the total perpendicular size of the beam, although the radial profile of the beam current can be modified by the action of whistlers. All nonlinearity is held in the electron motion; the drift approxi-

---

[1] This article was submitted by the authors in English.

mation is considered for the motion in the direction perpendicular to $\mathbf{B}_0$. The evolution of the emitted cylindrical whistlers is characterized by slow variations in the spatial wave structure along the distance z from the injector or, similarly, by slow changes in the parallel wave numbers.

A packet of M sheared whistlers with frequencies ω_m below the electron gyrofrequency ω_c and well above the low hybrid frequency ω_{lh} is considered ($\omega_c \ll \omega_p$, where ω_p is the electron plasma frequency); the whistler parallel wave number k_{zm} is much smaller than the perpendicular one, $k_{zm} \ll k_{\perp m}$. This allows one to describe electromagnetic wave fields using only the potentials A_z and φ; the perpendicular component $\mathbf{A}_\perp$ of the vector potential is small and can be expressed with the help of A_z. At a given ω_m, there are two resonant whistlers with the same k_{zm} (satisfying the Cherenkov resonance condition $k_{zm} v_{bz} = \omega_m$, where v_{bz} is the parallel beam velocity) and with two different perpendicular wave numbers k_{1m} and k_{2m}. The properties of whistler dispersion allow the beam to interact simultaneously with several waves having the same phase velocity but different ω_m and $k_{\perp m}$. The situation considered here is realistic, because spectral analysis of the modulated current of the beams injected from guns aboard satellites or in vacuum chambers typically exhibits not only the modulation frequency but also higher harmonics [2, 9]; moreover, modulation at different frequencies can also be applied simultaneously to the beam density [9].

Since the beam is thin (i.e., $k_{\perp m} r_b \ll 1$), all fields and potentials inside and outside the beam can be described in terms of potential amplitudes at the beam center, $\Psi_m = \Theta_{1m}(z) H_{1m} + \Theta_{2m}(z) H_{2m}$, where $\Theta_{im}(z)$ are slowly varying amplitudes of cylindrical waves and $H_{im} \equiv H_1^{(i)}(k_{im} r_b)$ are Hankel functions. Then, using Maxwell equations and matching conditions at the beam boundary with the conditions of free wave propagation to infinity, one can find M equations describing the self-consistent nonlinear evolution of whistler amplitudes along the beam, with a slow modulation of the parallel beam current j_{bz} as a source term:

$$\frac{\partial \Psi_m}{k_{zm} \partial z} + \kappa_m \Psi_m = -i \frac{2\pi v_{bz}}{\omega_p^2} \langle j_{bz, m} \rangle$$

$$= i \frac{2\pi e n_b v_{bz}^2}{\omega_p^2} \frac{1}{N} \sum_{j=1}^{N} e^{-i\theta_{j,m}}, \qquad (1)$$

where n_b is the initial beam density and e the electron charge; N is the total number of beam macroparticles; and $\theta_{j,m} = k_{zm} z_j - \omega_m t \equiv m\theta_j$, where $\theta_j = k_{z1} z_j - \omega_1 t$, is the phase of particle j in the field of the wave harmonic m. The r_b- and $k_{\perp m}$-dependent complex factor κ_m describes new effects of energy loss through the wave emission out of the beam to infinity (linear effective damping process). The analogy with the effective dissipation through collisions is not full: whereas $\text{Re}(\kappa_m)$ represents the rate of emission, $\text{Im}(\kappa_m)$ controls the reversible exchange of the wave-field energy inside the beam with that of the outside waves. The right-hand side of (1) describes the nonlinear interaction of the harmonic m with the resonant electrons; it results from the averaging of the beam current over the beam cross section. The slow evolution of the current is due to the variations of the particle phases θ_j as a result of the parallel motion of electrons in the field of M waves

$$\frac{d^2\theta_j}{dz^2} = -\frac{ek_{z1}}{m_e v_{bz}^2}\left(E_z + \frac{B_\theta E_\theta + B_r E_r}{B_0}\right) \simeq m$$

$$= 1\sum_{1}^{M} a_m(r)\Psi_m e^{im\theta_j} + \text{c.c.}, \qquad (2)$$

where m_e is the electron mass; $E_{r,\theta,z}$ and $B_{r,\theta,z}$ are, respectively, the total electric and magnetic fields at the particle position (r, θ, z); and $a_m(r)$ depends on the parameters of the beam-plasma system.

A similar model can describe the simple and well-studied case of electrostatic waves in a collisional plasma. In the normalized form, the evolution of the complex amplitude of the wave electric field $E_k = \mathcal{E}_k e^{iv_{bz}(k-k_0)t}$ and the motion of beam electrons can be presented as

$$\left(\frac{d}{d\tau} + \delta_k\right) A_k = \frac{1}{N}\sum_{j=1}^{N} e^{-ik'\theta_j},$$

$$\frac{d^2\theta_j}{d\tau^2} = -\sum_k A_k e^{ik'\theta_j} + \text{c.c.}, \qquad (3)$$

where $A_k = \eta^2 E_k / \sqrt{n_0 m_e v_{bz}^2}$ and $\eta = (n_b/n_0)^{-1/3}$; n_0 is the background plasma density; $\delta_k = \eta[\nu_c - i(\omega_k - v_{bz}k)]/\omega_{k_0}$, where ν_c is a collision frequency; k_0 is the Cherenkov resonance parallel wave number, $k' = k/k_0$; $\theta_j = k_0 z_j - \omega_{k_0} t$ is the phase of the particle j in the frame moving with velocity v_{bz}; and $\tau = \omega_{k_0} \eta t$. After proper normalization, equations (1), (2), and (3) take a very similar form characteristic of the dissipative beam–wave packet system.

The results of numerical calculations (solutions of the systems of equations) show various stages in the evolution of both above-mentioned dissipative systems. During the so-called initial stage, the waves grow according to the linear instability, saturate in amplitude, and begin to trap beam particles. During the trapping process, typical vortices appear in the phase spaces; some of them evolve further into clumps or electron bunches localized in space and velocity. Then, in contradiction to the well-known case of a conservative system (no dissipation), the energy lost by the beam to the waves cannot be returned to it because of the irrevers-
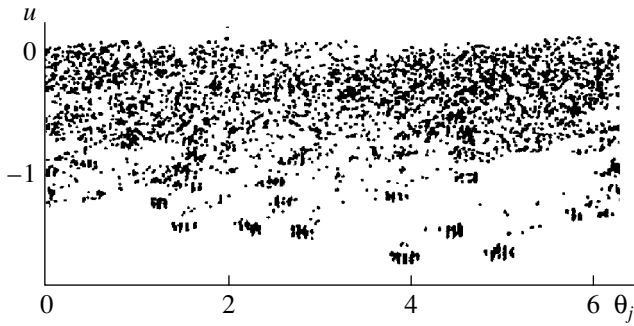
Fig. 1. Thin beam interaction with a packet of $M = 20$ whistlers. Electron dynamics in the $\theta_j - u$ phase space, where u and θ_j are the normalized parallel velocity of electrons in the frame moving with the initial beam velocity v_{bz} and their total phase, respectively. The uniform initial particle distribution, as well as the dimensionless parameters corresponding to active space experiments, are used; $M = 20$, $N = 6000$, and $n_b/n_0 \simeq 0.02$.

ible loss of wave energy and momentum: no quasi-periodic energy exchange between the waves and the trapped particles is observed. At the same time, the phase velocity of waves is self-adjusted owing to a nonlinear shift of their parallel wave number, so that Cherenkov resonance with bunched particles holds. The stable nonlinear structures thus formed, the so-called bunches, are continuously decelerated (slowing down of the beam); however, as the rate of energy transfer from beam to waves decreases, they are damped.

In the case of a single quasi-monochromatic whistler, the continuous bunch-deceleration and Cherenkov resonance-tuning processes can be explained with the help of a simple model treating bunches as nonlinear resonant structures. At the asymptotic stage of the interaction, a well-formed bunch can be considered as a single particle with weight $n_{tr} = N_{tr}/N$ proportional to the number N_{tr} of particles it contains; the current modulation is only due to the bunched particles. As confirmed by the numerical solution, the wave and the bunch remain in phase; i.e., $\theta_b + \psi + \pi/2 = \varphi \approx \text{const}$. Then, the bunch interaction with the dissipating wave follows from the normalized form of (1), (2)

$$|A| \simeq -\frac{n_{tr}}{v}\sin\varphi, \quad \frac{dv}{d\tau} \simeq -\frac{n_{tr}}{v}\sin 2\varphi,$$

$$\frac{dv^2}{d\tau} \simeq -2n_{tr}\sin 2\varphi \simeq \text{const}, \tag{4}$$

where $A = |A|e^{i\psi}$ is the normalized wave amplitude and $v \simeq -d\psi/d\tau$ is the nonlinear shift of phase velocity. Even in the case of single wave, not only one but several bunches with different velocities can exist; they are resonant with the waves present in the Fourier spectrum. Indeed, slow changes in the main wave characteristics can be considered as a result of the superposition of several waves whose wave numbers differ slightly. The case of the beam–wave packet interaction is much

more complicated, because the different waves can successively trap electrons and, as a result, form a wider variety of bunches (in size, velocity spread, number of particles, and deceleration); these can be accelerated or decelerated according to their phase matching with waves. As the bunch velocity decreases continuously, the bunched electrons can start to interact with the waves of smaller phase velocities than the phase velocity of the initial trapping wave. The bunches can catch up with each other and merge to form bigger bunches. Each formed bunch makes a finite contribution to the amplitude A_m of harmonic m, according to the phenomenological estimation [derived from (1), with δ_m standing for the normalized form of κ_m]:

$$A_m \simeq i\sum_{l=1}^{M_b} \frac{mn_l e^{-im\theta_b}}{(i\partial\theta_b/\partial\tau + m\delta_m)}, \tag{5}$$

where n_l is the relative number of particles inside the bunch l, M_b is the total number of bunches, and θ_b is the phase of bunch l (all particles it contains have roughly the same phase). If the bunches formed have similar characteristics, their behavior with respect to the waves is roughly equivalent, and they can all be resonant with waves. In contrast, if a certain bunch contains many more electrons than the others do, it dominates the system dynamics, because only it interacts strongly with the waves. The other bunches participate weakly in the radiation process, even though they are in resonance with waves. But, inasmuch as each A_m is the sum of resonance contributions from all bunches [see (5)], the nonvanishing (on average) resonance deceleration force acting on the particles in bunch l is $F_l = d^2\theta_b/d\tau^2$; since the phases of all waves are well correlated, this force is proportional to the relative number of particles in the bunch:

$$F_l \propto \text{Re}\left[\sum_m iA_m e^{im\theta_b}\right] \propto n_l.$$

At the asymptotic stage of the interaction process, the beam particles are eventually separated into two distinct groups: the dynamically stable bunches continuously decelerated in resonance with the waves and the stochastic population of nonresonant electrons, the so-called bulk executing more or less pronounced diffusion to lower velocities. The number of particles in each bunch, as well as in the bulk, is established during the trapping by waves and the subsequent bunch formation; it depends on the beam parameters and initial conditions. This picture is different from that usually expected from the quasilinear theory, where the system evolves asymptotically toward a plateau distribution through the velocity diffusion; in our case, additional nonlinear stable structures are present in the velocity distribution, allowing the beam to radiate energy out of its volume at a significant distance from the injection point. Thus, the strong effective dissipation can prevent the stochastic phase mixing required for the validity of the quasilinear theory and to keep the phases of all
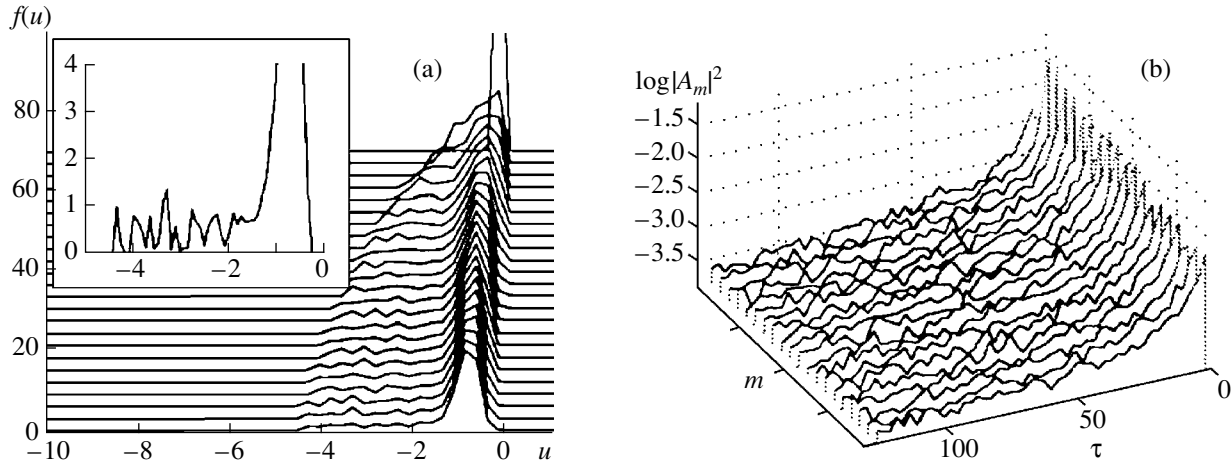
Fig. 2. Thin-beam interaction with a packet of $M = 20$ whistlers. Variation as a function of the normalized distance τ to the injector ($0 < \tau < 125$) of (a) the parallel velocity distribution $f(u)$ ($\tau = 0$ for the upper curve); the inset on the left upper corner represents a zoom of $f(u)$ at the asymptotic stage $\tau = 125$; a diffusion plateau together with bunched structure are seen; (b) the normalized electromagnetic energy $|A_m|^2$ (in logarithmic scale) carried by the M waves m. Parameters are the same as in Fig. 1.

waves well correlated. The sequences of bunches (a strongly modulated electron beam) propagating together with the forced electric field perturbations (modulated wave packet) can be considered as nonlinear van Kampen modes in a plasma including dissipation.

The main features of the beam–wave system evolution are shown in Figs. 1 and 2 illustrating the results of numerical calculations of the interaction of a thin modulated electron beam with a packet of whistlers in the presence of dissipative effects (wave radiation out of the bounded beam volume). Figure 1 shows the electron phase space at the stage where most bunches are well formed after trapping by the wave packet and well separated from the nonresonant bulk. In Fig. 2, one can see the evolution of the parallel beam velocity distribution with the distance to the injector, exhibiting bunch deceleration, bulk heating, velocity diffusion, and the formation of a plateau with fine bunched structures, as well as the electromagnetic energy carried by the waves.

In conclusion, the numerical calculations of the beam interaction with a finite number of waves in the presence of effective dissipation have shown that, independently of the dissipation type and the nature of the waves considered, the nonlinear evolution of the particle distribution has a tendency to self-organization, leading to the formation of highly concentrated electron structures. These bunches of resonant particles are decelerated continuously by the friction on the waves, and their dynamics shows noticeable stability in the time range exceeding several characteristic times of their formation. When the number of waves in the packet is large and the wave spectrum is continuous, a quasilinear diffusion of particles in the velocity space and plateau formation in the velocity distribution are usually expected to occur during the beam relaxation

stage. In the strongly dissipative case, however, our calculations show the coexistence, in the velocity distribution, of a wide, very low plateau together with the small peaks (at lower velocities) corresponding to the stable electron bunches that typically contain about 1–10% of the total number of particles. On the other hand, the plateau itself exhibits fine structure consisting of a large set of small and almost indistinguishable bunches. At the asymptotic stage of evolution, the deceleration rate of bunches and, correspondingly, their whistler emission rate are proportional to the number of particles they contain. At the same time, each wave is supported by all bunches, and, on average, the waves in the packet have almost the same amplitudes, although not the same emission rates (which in the whistler case are proportional to the wave frequency). If the total number of particles gathered in bunches is not too small, the whistler energy emitted during the long asymptotic stage of beam relaxation (and the total loss of beam energy) can exceed the whistler emission in the initial stage of the interaction (i.e., near the injector), although the latter is much more intense. Therefore, it is essential to find the way to control the amount of particles organized into bunches in order to increase the emission efficiency. Our calculations show that one of the possibilities for achieving this aim is to premodulate the beam at one or several frequencies.

REFERENCES

1. C. Krafft *et al.*, Phys. Rev. Lett. **72**, 649 (1994).
2. M. Starodubtsev and C. Krafft, Phys. Rev. Lett. (1999) (in press).
3. D. A. Whelan and R. L. Stenzel, Phys. Rev. Lett. **47**, 95 (1981).
4. T. Neubert and P. M. Banks, Planet. Space Sci. **40**, 153 (1992).
5. J. R. Winckler, Rev. Geophys. Space Phys. **18**, 659 (1980).
6. W. M. Farrell *et al.*, J. Geophys. Res. **94**, 443 (1989).
7. J. Lavergnat *et al.*, Ann. Geophys. (C.N.R.S.) **36**, 323 (1980).
8. P. M. Banks and W. J. Raitt, J. Geophys. Res. **93**, 5811 (1988).
9. Z. Nemecek *et al.*, J. Geophys. Res. **102**, 2201 (1997).
10. T. Neubert *et al.*, J. Geophys. Res. **92**, 255 (1987).
11. J. A. Miller *et al.*, J. Geophys. Res. **102**, 14631 (1997).
12. G. A. Dulk *et al.*, J. Geophys. Res. **103**, 17223 (1998).
13. T. M. O'Neil *et al.*, Phys. Fluids **14**, 1204 (1971).
14. N. G. Maziborko *et al.*, Plasma Phys. **14**, 591 (1972).
15. V. Pivavorov *et al.*, J. Geophys. Res. **17**, 17515 (1995).
16. A. S. Volokitin *et al.*, Phys. Plasmas **4**, 1 (1997).
17. C. Krafft and A. S. Volokitin, Phys. Plasmas **5**, 4243 (1998).
18. C. Krafft and A. S. Volokitin, J. Plasma Phys. **61**, 275 (1999).
19. A. A. Ivanov *et al.*, Zh. Éksp. Teor. Fiz. **63**, 1678 (1973) [Sov. Phys. JETP **36**, 887 (1973)].

<div align="center">══════════════ CONDENSED MATTER ══════════════</div>

Solid-Phase Reactions, Self-Propagating High-Temperature Synthesis, and Order–Disorder Phase Transition in Thin Films

V. G. Myagkov*, L. E. Bykova*, G. N. Bondarenko**, V. S. Zhigalov*, A. I. Pol'skiĭ*, and F. V. Myagkov*

**Kirenskiĭ Institute of Physics, Siberian Division, Russian Academy of Sciences,
Akademgorodok, Krasnoyarsk, 660036 Russia*
**Institute of Chemistry and Chemical Technology, Siberian Division, Russian Academy of Sciences, Krasnoyarsk, Russia
Received January 19, 2000

Abstract—The results of experimental studies of self-propagating high-temperature synthesis in double-layer Cu/Au thin-film systems are presented. It is shown that the synthesis initiation temperature for a Cu/Au film is determined by the order–disorder phase-transition temperature in the Cu–Au system. The order–disorder transition temperature for thin films is found to be lower than for the bulky samples. It is assumed that the temperatures of initiation of solid-phase reactions in thin films can be associated with the structural phase-transition temperatures. © 2000 MAIK "Nauka/Interperiodica".

PACS numbers: 81.30.Hd; 82.65.-i

Solid-phase reactions in thin films proceed at temperatures considerably lower than the relevant temperatures in bulky samples. The majority of solid-phase reactions occur at the interfaces between thin films at temperatures as low as 400–800 K (see, e.g., [1, 2]). However, on long aging, the compounds can form at the contact surface even at room temperature [3]. It is believed that diffusion along the grain boundaries is a dominant mechanism of solid-phase reactions in thin films, because it is several orders more efficient than bulk diffusion. Because of this, diffusion along the grain boundaries and a high defectiveness of thin films may be responsible for considerable mass transport at low temperatures [1]. Since the solid-phase reactions in thin films proceed under nonequilibrium conditions, the phase diagram, as a rule, is not invoked for an analysis of the composition of reaction products and the temperatures of their formation. In practice, it is important to know the formation temperatures, because the thin-film technologies are widely used in microelectronic devices. These devices are often fabricated and operate at temperatures close to the temperature of initiation of solid-phase reactions in thin-film elements. Among the diversity of solid-phase reactions in thin films, there is a class of reactions that occur during the course of fast thermal annealing (see, e.g., [4]). Rapid thermal annealing is part of a rapid isothermal treatment; it amounts to the fast heating of film samples to a certain temperature followed by annealing for 1–100 s at this temperature and subsequent cooling [5]. It is shown in [6, 7] that the solid-phase reactions in thin films can proceed in the self-propagating high-temperature synthesis (SHS) regime. SHS is initiated in double-layer films when the sample temperature T_S

exceeds the initiation temperature T_0 ($T_S > T_0$). SHS is a surface combustion wave propagating along the film surface. At temperatures near the initiation temperature, the SHS-front velocity is equal to $\sim (2\text{–}10) \times 10^{-2}$ m/s. Because of this, the traveling time for the SHS wave in the experimental samples is equal to 5–15 s. This implies that many solid-phase reactions occurring in the course of rapid thermal annealing are the SHS reactions. There are two SHS types in thin films. For the first one, the reaction products contain compounds and only a single SHS wave occurs, as in the case of SHSs in powders. For the second SHS type, the passage of the combustion wave at $T_S > T_0$ and the lowering of the film temperature to a temperature below the initiation temperature $T_S < T_0$ is followed by the passage of a second front that is inverse of the SHS front and results in phase layering in the sample. In [8, 9], the SHS of the second type is referred to as multiple SHS (MSHS). MSHS is a reversible structural phase transition corresponding to the transition through the eutectic temperature T_E^M of bulky samples [9]. However, a film analogue T_E^f of the T_E^M temperature is lower than the eutectic temperature T_E^M of the bulky samples ($T_E^f < T_E^M$). It is conceivable that efficient heat removal to a support reduces the temperature of solid-phase reactions in thin films. Unexpectedly, multiple SHS occurs in the solid phase, where it proceeds with an exceedingly low activation energy [10]. In this case, the compounds are formed at the temperature $T_0 = T_E^f$ of SHS initiation. It is assumed that the mechanism of phase layering induced by the passage of the front of multiple SHS is related to the mechanisms of phase layering caused by eutectic crystallization and eutectoid or spinodal
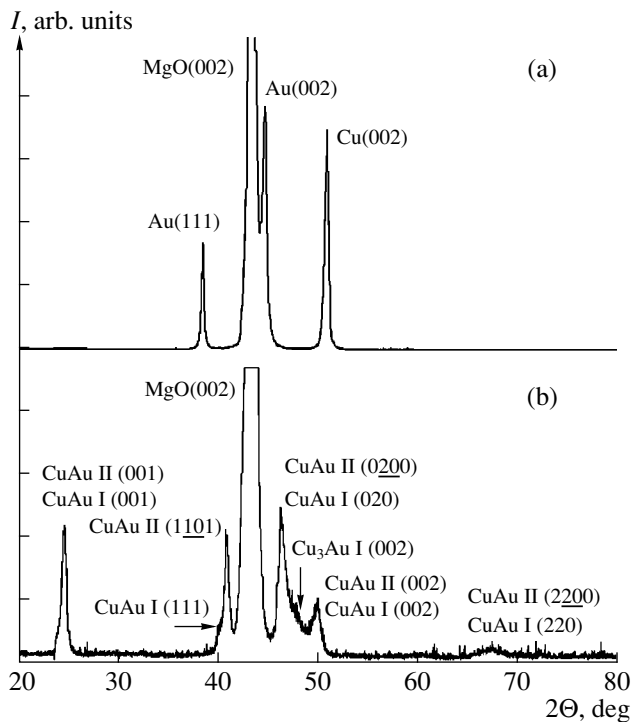
Fig. 1. X-ray diffraction patterns of a double-layer Au(80 nm)/Cu(55 nm)/MgO(001) film sample; (a) initial sample and (b) after the fast thermal annealing cycle.

decomposition [9]. The result obtained implies that the compounds can form in thin films upon other reversible solid-phase transformations, among which the order–disorder phase transition is most familiar.

This work is devoted to studying SHS in the double-layer films for which the reaction products can undergo the order– disorder phase transition. The study was carried out on a Cu–Au system that is classical as regards the ordering phenomenon. The purpose of this work was to demonstrate that the temperature T_0 of initiation of the solid-phase reactions between the gold and copper layers is determined by the Kurnakov temperature T_K of a bulky Cu–Au system. The distinctive feature of the Cu–Au system [11, 12] is that, depending on the concentration, the ordered CuAu (superstructure $L1_0$) and Cu_3Au (superstructure $L1_2$) phases form modulated CuAu‖ and Cu_3Au‖ structures at elevated temperatures in a narrow interval of 25–80 K. For example, CuAu‖ is a one-dimensional modulated structure composed of ten oriented tetragonal CuAu‖ cells arranged along the b-axis. From the phase diagram [11] it follows that the Kurnakov temperature T_K changes from 510 to 683 K in the concentration range of 40–60 at. % Au. It is significant that the Cu–Au system exhibits no solid-phase structural transformations other than the ordering phenomenon.

Experimental samples were thin-film systems comprised of copper and gold layers sequentially deposited

on glass mica supports or on a freshly cleaved MgO (001) surface. To produce single-crystal layers on the MgO (001) surface, the first layers were deposited at temperature $T_S = 500$ K. To avoid reaction between the layers, the second layer was deposited at room temperature. The layer thicknesses were chosen in such a way that the completely reacted samples contained 40–60 at. % Au. The Au/Cu samples thus obtained were placed on a heater and heated at a rate of no less than 20 K/s up to the SHS-initiation temperature T_0, which turned out to be equal to 520–540 K. The initiation temperature $T_0 = 520$–540 K did not depend on the layer thicknesses, which determined the concentration in the reacted sample. In the samples on glass mica supports, the SHS reaction exhibited weakly pronounced autowave behavior. The coefficient of reflection from the sample surface changed, allowing visual observation of the course of the reaction. For the samples on the MgO (001) support, the SHS reaction was weakly detectable. Because of this, the samples were subjected to fast thermal annealing consisting of heating to $T_S = 570$ K $> T_0$, exposure to this temperature for 15 s (the time required for the reaction), and slow cooling at a rate of ~ 0.05 K/s.

Figure 1 shows the X-ray diffraction patterns of the Au(80 nm)/Cu(55 nm)/MgO(001) sample corresponding to an approximately 1 : 1 gold-to-copper atomic ratio in the reaction products. The initial samples consisted of epitaxial Cu layers with the (001) orientation parallel to the MgO (001) surface. The upper Au layer grew in two preferable orientations, (001) and (111) (Fig. 1a). The reflections from Au and Cu disappeared after the reaction, suggesting that the layers completely reacted. The X-ray patterns of the reacted Au(80 nm)/Cu(55 nm)/MgO(001) samples show reflections from the ordered tetragonal CuAu‖ phase having the (001), (111), (010), and (110) orientations, as well as the reflections from the orthorhombic CuAu‖ phase with the (100), ($1\underline{10}1$), ($0\underline{10}0$), and ($1\underline{10}0$) orientations parallel to the MgO (001) surface. The Cu_3Au phase with the (100) orientation can form in the reaction products (Fig. 1b). On the whole, the compounds formed in this concentration range corresponded to the equilibrium phase diagram [12]. The relative electrical resistance $R(T_S)$ of the double-layer Au(80 nm)/Cu(55 nm)/MgO(001) sample is shown in Fig. 2 as a function of the support temperature T_S for three successive cycles of fast thermal annealing.

The measurements of electrical resistance $R(T_S)$ (Fig. 2) showed that the smooth change in $R(T_S)$ was interrupted at $T_S = T_0 \sim 530$ K because of SHS onset in the film sample at $n = 1$. In subsequent cycles ($n > 1$), the smooth $R(T_S)$ dependence was again interrupted at $T_S \sim 530$ K. However, it is caused by the order–disorder transition in CuAu‖ and CuAu‖. In the SHS and the order–disorder-transition regions, the resistance exhibits a slight hysteretic behavior typical of the order–disorder transitions. The slopes of hysteresis branches to

the T_S-axis in the temperature interval (T_{1K}^f, T_{2K}^f) likely correspond to the reversible structural CuAu| $\longleftrightarrow$ CuAu‖ transitions, while the temperature T_{2K}^f corresponds to the CuAu‖ $\longleftrightarrow$ γ-solid solution transition. It follows from Fig. 2 that the synthesis temperature T_0 for the thin contacting Cu and Au films coincides with the Kurnakov temperature T_{2K}^f of the CuAu films ($T_0 = T_{2K}^f$). However, the T_{2K}^f temperature for the films of equiatomic composition studied in this work turned out to be lower than the Kurnakov temperature of the bulky samples ($T_{2K}^f < T_K$). A plausible explanation is that the temperature curve for the Kurnakov point in thin films is independent of the concentration and goes lower than the pertinent curves for the bulky samples, much as the T_E^f temperature is lower than the eutectic temperature T_E^M. An alternative explanation is that synthesis between the gold and copper layers is initiated at the temperature corresponding to the minimum order–disorder-transition temperature in the phase diagram. The $R(T_S)$ curves shown in Fig. 2 are similar to those for the temperature-dependent resistance of a support at different cycles of initiation of the MSHS fronts [9]. It was shown in [6, 7] that SHS in the thin double-layer films is also initiated upon the deposition of one layer upon the other if the support temperature T_S in the course of deposition of the second layer is higher than the initiation temperature ($T_S > T_0$). In this case, the synthesis in the Au/Cu film systems is initiated at the same temperature $T_0 = 520$–540 K. Note that this method was used for preparing the samples on a fresh NaCl (001) cleavage in the early studies of long-period ordering in CuAu‖ [13]. Nevertheless, the temperature T_0 of synthesis initiation between the Au film and Cu film deposited on top of it was found not to correlate with the ordering temperature. The phase diagrams of the Co–Pt and Au–Cu systems are similar in the equiatomic composition region. In the region of a homogeneous ordered CoPt phase, the Kurnakov temperature changes from 750 to 1070 K, with the maximum value corresponding to the stoichiometric composition. The solid-phase reactions in the Co/Pt/MgO(001) multilayers are initiated at temperatures $T > 750$ K and result in the ordered CoPt phase [14]. It is shown in [15] that the solid-phase reactions in the double-layer and multilayer Co/Pt films proceed in the SHS regime, with the initiation temperatures $T_0 = 770$–820 K coinciding with the temperature of phase ordering in CoPt [16]. This implies that the temperature of initiation of the interlayer synthesis in Co/Pt is determined by the Kurnakov temperature, as in the case of the Au/Cu films. Hence it follows that the initiation temperatures for the film systems exhibiting solid-phase reactions can be associated not only with the order–disorder-transition temperature in the reaction products but also with the temperatures of the other structural phase transformations.
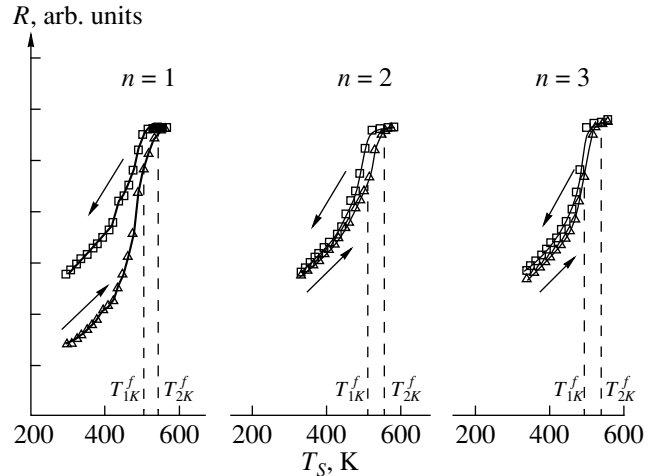
Fig. 2. Electrical resistance $R(T_S)$ of a double-layer Au(80 nm)/Cu(55 nm)/MgO(001) film sample vs. support temperature T_S for three successive fast thermal annealing cycles. The interruption of the smooth behavior of $R(T_S)$ in the temperature interval $(T_{1K}^f, T_{2K}^f) = 520$–540 K at the first cycle is associated with synthesis onset between the Au and Cu layers. In subsequent cycles, these changes are caused by the order–disorder phase transitions in the AuCu alloy.

In summary, it is shown that the initiation temperature of the Au/Cu film systems is determined by the Kurnakov temperature for the Au–Cu system. This implies that the chemical mechanisms of ordering and synthesis are the same and have a long-range nature. The long-range forces, together with the elastic forces, may be responsible for the formation of the long-period modulated phases that appear upon ordering, spinodal and eutectic decompositions, in the polytypic structures, etc. The results of this study may be of practical importance, because the phase diagram can be used to determine the types of solid-phase reactions and the corresponding initiation temperatures.

ACKNOWLEDGMENTS

REFERENCES

1. *Thin Films: Interdiffusion and Reactions*, Ed. by J. M. Poate, K. Tu, and J. Meier (Wiley, New York, 1978; Mir, Moscow, 1982).

2. L. A. Clevenger, B. Arcort, W. Ziegler, *et al.*, J. Appl. Phys. **83**, 90 (1998); M. Zhang, W. Yu, W. H. Wang, *et al.*, J. Appl. Phys. **80**, 1422 (1996); J. D. Guo, F. M. Pan, M. S. Feng, *et al.*, J. Appl. Phys. **80**, 1623 (1996); H. S. Venugopalan, S. E. Mohney, B. P. Luther, *et al.*, J. Appl. Phys. **82**, 650 (1997); J. S. Huang, K. N. Tu, *et al.*, J. Appl. Phys. **82**, 639 (1997); W. H. Wang, W. K. Wang, *et al.*, J. Appl. Phys. **76**, 1578 (1994); B. I. Boyanov,

D. T. Goeller, D. E. Sayers, *et al.*, J. Appl. Phys. **84**, 4285 (1998); Q. Z. Liu, L. S. Yu, F. Denf, *et al.*, J. Appl. Phys. **84**, 881 (1998); J. P. Gambino, B. Cunningham, P. DeHaven, *et al.*, J. Appl. Phys. **82**, 6073 (1997); L. Balazc, V. Freury, F. Duclos, *et al.*, Phys. Rev. E **54**, 599 (1996).

3. V. Simic and Z. Marincovic, J. Mater. Sci. **33**, 561 (1998).

4. L. J. Chen, I. W. Wu, J. J. Chu, *et al.*, Appl. Phys. **63**, 2778 (1988); E. G. Colgan, C. Cabral, Jr., and D. E. Kotecki, J. Appl. Phys. **77**, 614 (1995).

5. R. Singh, J. Appl. Phys. **63**, R59 (1988).

6. V. G. Myagkov and L. E. Bykova, Dokl. Akad. Nauk **354**, 777 (1997).

7. V. G. Myagkov, V. S. Zhigalov, L. E. Bykova, and V. K. Mal'tsev, Zh. Tekh. Fiz. **68**, 58 (1998) [Tech. Phys. **43**, 1189 (1998)].

8. V. G. Myagkov, Dokl. Akad. Nauk **364**, 330 (1999) [Dokl. Phys. **44**, 45 (1999)].

9. V. G. Myagkov, L. E. Bykova, and G. N. Bondarenko, Zh. Éksp. Teor. Fiz. **115**, 1754 (1999) [JETP **88**, 963 (1999)].

10. V. G. Myagkov and L. E. Bykova, Dokl. Akad. Nauk (in press).

11. C. S. Barrett and T. B. Massalskiĭ, *Structure of Metals. Crystallographic Methods, Principles and Data* (Pergamon, New York, 1980; Metallurgiya, Moscow, 1984), Chap. 1.

12. N. M. Matveeva and É. V. Kozlov, *Ordered Phases in Metallic Systems* (Nauka, Moscow, 1989).

13. H. Sato and R. S. Toth, Phys. Rev. **124**, 1833 (1961).

14. B. M. Lairson, M. R. Visokay, R. Sinclair, and B. M. Clemens, J. Magn. Magn. Mater. **126**, 577 (1993); B. M. Lairson and B. M. Clemens, Appl. Phys. Lett. **63**, 1438 (1993).

15. V. G. Myagkov, L. A. Li, L. E. Bykova, *et al.*, Fiz. Tverd. Tela (St. Petersburg) (in press).

16. K. Barmak, R. A. Ristau, K. R. Coffey, *et al.*, J. Appl. Phys. **79**, 5330 (1996).

Translated by V. Sakun

================= **CONDENSED MATTER** =================

Heavy-Fermion States in Non-Fermi-Liquid Impurity Metals

L. A. Manakova

Russian Research Centre Kurchatov Institute, pl. Kurchatova 1, Moscow, 123182 Russia
Received December 16, 1999; in final form, February 10, 2000

Abstract—It is shown that a new type of instability of a non-Fermi-liquid state to the interband scattering of multiparticle excitations can dominate the formation of heavy-fermion states in non-Fermi-liquid metals doped with unstable-valence f impurities. A new mechanism is proposed for the formation of a small energy scale and pseudogaps near the Fermi level in a mixed-valent state. © *2000 MAIK "Nauka/Interperiodica".*

PACS numbers: 72.10.Fk; 72.15.Qm; 73.20.-r; 73.40.Gk

1. Historically, the diluted U compounds ($U_xY_{1-x}Pd_3$, $U_xTh_{1-x}Ru_2Si_2$, see reviews [1, 2]) were the first heavy-fermion (HF) systems to exhibit non-Fermi-liquid (NFL) behavior. The anomalous temperature dependences of their heat capacity and magnetic susceptibility, as well as some other characteristics were successively described by the two-channel quadrupolar Kondo model [2]. However, most of the U compounds have mixed-valent nature (recent data in [3, 4]). It should be noted that the on-site NFL effects can likely play the important role in the "concentrated" systems ($U_{1-x}Th_xBe_{13}$ [1], UBe_{13} [5]).

Bearing this in mind, it was of interest to suggest a unified mechanism for the explanation of both the NLF properties generated by the on-site two-channel Kondo scattering and the possibility of the mixed valence to exist. It should be emphasized that the role of the NFL-state instabilities in the mechanisms of formation of heavy fermions still remains to be studied. Two mechanisms of the NFL-state instability in the two-channel quadrupolar Kondo model were previously known. In [5], the instability was attributed to the Jahn–Teller distortions of impurity sites and in [6], to the anisotropy of scattering channels. It was demonstrated in [7, 8] that the NFL state may be unstable (i) to the multiparticle-excitation scattering induced by tunneling in quantum-dimensional structures [7] and (ii) to the scattering of NFL excitations with different z-projections of quadrupole moment in a metal with deep orbitally degenerate d or f levels [8].

In this work, a unified mechanism is proposed for obtaining both mixed- and near-integer-valence HF states in NFL metals. The mechanism is based on the on-site NFL effects for a deep orbitally degenerate level and the new type of NFL-state instability to the scattering of multiparticle excitations by the electronic states of the atomic quasicontinuum. The scattering and the scattering-induced instability are key words in the proposed mechanism. The temperature $T = 0$ is considered in this study.

2. It is known that ions with unfilled d or f shells partially hold their atomic properties in a crystal. This is possible, first, because of the presence of a centrifugal barrier separating the regions of atomic forces and lattice potential and, second, because the symmetry of the electronic states of unfilled shells is different from the conduction-band states. In this work, the unstable-valence atoms are assumed to have an energy spectrum with two unfilled shells formed by a deep f level and the quasicontinuum states under the centrifugal barrier (A-continuum or A-subband). The latter can form from the excited $\tilde{f}$ states and the d states resonant with the Fermi energy of the conduction band (B-band). Such an impurity model was considered in [9] for a deep level with the degree of degeneracy much greater than unity. In this work, a quadrupolar nonmagnetic Γ_3 crystal-field doublet is taken as a deep level. The Γ_3 doublet is the ground state of the U^{4+} ion. The row numbers of the irreducible representation of a point group $\mu_\Lambda = \pm 1$, $\Lambda = \Gamma_3$ are the quantum numbers μ of an electron in the Γ_3 level. Two values of the quantum number μ_Λ correspond to the two projections of the quadrupole moment on the z-axis. The components of the quadrupole moment form the pseudospin operator that is responsible for the scattering of the conduction electrons. In the U compounds, the Γ_3 states are hybridized with the conduction-band states of the Γ_8 and $\bar{\Gamma}_8$ symmetries. The hybridization of the deep Γ_3 doublet with the conduction-band states in combination with a strong Coulomb repulsion in the Γ_3 level results, after applying the Schrieffer–Wolff transformation, in the effective interaction between the impurity state and conduction electrons. Two-channel quadrupolar exchange scattering is the dominant interaction under the following conditions. First, the interaction matrix elements $V_{\mu\mu'}(\mathbf{k}, \mathbf{k}')$ should be spatially nonlocal and be nonzero if $\mu \neq \mu'$. Both these conditions can be fulfilled if the hybridization matrix elements are spatially nonlocal [7, 8]. Second, it is known [5] that Kondo scattering changes the z-projection of the quadrupole moment, but the quantum number $\alpha = \pm$ for Γ_8 and $\bar{\Gamma}_8$, respectively, is retained and specifies the scattering-channel index in

the two-channel quadrupolar Kondo model. In addition to two-channel quadrupolar exchange scattering, we shall take into account potential scattering of the multiparticle conduction-band states by the A-subband states. This scattering results in the NFL-state instability and is crucial in the proposed mechanism. In terms of the partial states with quantum numbers (Λ, μ, α, ε), where $\varepsilon = v_F k - \varepsilon_F$, k is the wave-vector magnitude and ε_F is the Fermi energy, the Hamiltonian of the system under consideration is written in the form $H = H_{00} + H_{sc} + H_{int} + h\hat{\tau}_\Lambda^z$, where h is the doublet splitting caused by the local distortions of the impurity site;

$$H_{int} = \sum_{\mu\mu'\alpha} \sum_{i = x, y, z} \iint d\varepsilon d\varepsilon' \rho_B(\varepsilon) \rho_B(\varepsilon') V_{i\alpha}^\Lambda(\varepsilon, \varepsilon')$$
$$\times a_{B\alpha\mu}^+(\varepsilon) \sigma_{\mu\mu'}^i a_{\alpha\mu'}(\varepsilon') \hat{\tau}_\Lambda^i, \tag{1}$$

$$\hat{\tau}_\Lambda^i = \sum_{\mu\mu' = \pm 1} d_{\Lambda\mu}^+ \sigma_{\mu\mu'}^i d_{\Lambda\mu'},$$

$$V_{i\alpha}^\Lambda(\varepsilon, \varepsilon') \sigma_{\mu\mu'}^i \sim \frac{V_{\mu\alpha}^{\Lambda*}(\varepsilon) V_{\mu'\alpha}^\Lambda(\varepsilon')}{\varepsilon_\Lambda},$$

$$H_{sc} = \sum_{\mu\alpha} \int_{-\infty}^{+\infty} d\varepsilon \rho_A(\varepsilon) \int_{-\infty}^{+\infty} d\varepsilon' \tilde{\rho}_B(\varepsilon') T_{AB\mu}^\Lambda(\varepsilon, \varepsilon')$$
$$\times a_{A\alpha\mu}^+(\varepsilon) \tilde{a}_{B\{\mu\}}(\varepsilon'), \tag{2}$$

where the operators $a_{\mu\alpha B, A}(\varepsilon)$, $a_{\mu\alpha B, A}^+(\varepsilon)$ describe the noninteracting states of the conduction band (B) and the atomic continuum (A); $d_{\Lambda\mu}^+$ creates an electron in the Γ_3 level with the pseudospin z-projection μ; $\hat{\sigma}^i$ are the Pauli matrices; $\varepsilon_F - E_\Lambda \equiv \varepsilon_\Lambda$; and $V_{\mu\alpha}^\Lambda(\varepsilon)$ are the hybridization matrix elements. The Hubbard repulsion at the impurity site is assumed to be the largest parameter in the problem. For simplicity, the terms with $\mu \neq \mu'$ are not included in H_{sc}. The $\tilde{a}_{B\{\mu\}}$} and $\tilde{\rho}_B(\epsilon)$ quantities describe the multiparticle states with quantum numbers $\{\mu\}$.

The system described by the Hamiltonian H involves two physical mechanisms generating singularities at or near the Fermi level. The interaction in (1) with $V_{i\alpha}^\Lambda \equiv V_i^\Lambda$ is responsible for the appearance of the NFL resonance at the Fermi level of the B-band. Moreover, scattering (2) of the NFL excitations by the A-subband states results in the new multiparticle Fermi-liquid (FL) resonances near the Fermi level. Using the results obtained in [7, 8], one can show that, with allowance made for interaction and scattering, the Green's function $G_{\Lambda\mu}(z) = \langle d_{\Lambda\mu} | (z - \hat{H})^{-1} | d_{\Lambda\mu} \rangle$ of the resonance Λ-level near the Fermi surface has the form

$$\hat{G}_{\Lambda\mu}(z) = \hat{G}_\Lambda^{(\pm)}(z) \frac{1 - \Sigma_{A\mu}(z) \Sigma_{B\mu}(z)}{D_\mu^{AB}(z)}. \tag{3}$$

As mentioned above, this expression contains singularities of two types. The Green's function $\hat{G}_\Lambda^{(\pm)}(z)$ describes the contribution from the NFL resonance. The second factor in (3) has simple poles that correspond to new FL resonances in the energy range of interest. As shown in [7, 8], the character of low-lying excitations depends heavily on the z-component V_z^Λ of the exchange interaction. At $\tilde{V}_z^\Lambda \equiv 2(V_z^\Lambda - \pi v_F) \gg V_{x, y}^\Lambda$ and $T_K \ll h$, where T_K is the exponential Kondo temperature, the NFL behavior is governed by the "X-rayedge" mechanism and the power-law energy dependences of the Green's functions, so that

$$\hat{G}_\Lambda^{(\pm)}(z) = A_{(\pm)} \sum_{j = 1, 2} \frac{\hat{\sigma}^0 \mp \hat{\sigma}^x}{W^{\alpha_s}(z + i\Gamma_j)^{1 - \alpha_s}};$$
$$\Gamma_1 = \Gamma_K \sim W \frac{\gamma_{\Lambda B}^2}{\varepsilon_\Lambda^2}; \quad \Gamma_2 = \delta \longrightarrow 0^+; \tag{4}$$

where $A_{(\pm)}$ are the phase factors for $\mathrm{Re}\, z \gtrless 0$, respectively (the Fermi energy is taken to be zero); the signs $\mp$ in the numerator correspond to $j = 1, 2$; $\gamma_{\Lambda B} = |V_{B\mu}^\Lambda|^2 \rho_{0B}$, $\rho_{0B} \sim 1/W$ is the density of states of the noninteracting conduction electrons, where the cutoff parameter W, as usual, is of the order of the B-band width $\alpha_s = (\delta_s/\pi)^2$; and δ_s is the phase shift in the scattering by the z-component of the exchange interaction. In (4), the splitting h is assumed to be much smaller than Γ_K (and all other energy scales that appear in what follows). It should also be noted that the applicability of a power law imposes a lower bound on the α_s values (see below). At $T_K \gg h$, the interaction involving $\tilde{V}_z^\Lambda$ is immaterial [2], the Kondo mechanism is operative, and the NFL behavior in the two-channel model is dictated by the presence of the impurity degrees of freedom nonhybridized with the conduction electrons.

The denominator in (3) is determined by the expression

$$D_\mu^{AB}(z) = 1 - \Sigma_{A\mu}(z) W_{B\mu}(z),$$
$$W_{B\mu}(z) = \Sigma_{B\mu}(z) + \Sigma_{B\mu}(z) \Sigma_{\mu B}(z) G_\Lambda^{(\pm)}(z).$$

The self-energy functions $\Sigma_{\nu\mu}(z) \Gamma\nu = A$ and B are written in the form of spectral decompositions of the electronic Green's functions for the A and B bands. Their energy dependences are determined by the respective densities of states at the Fermi level. In the problem under consideration, the function $\Sigma_{A\mu}(z)$ has no singularities at the Fermi level, so that $\mathrm{Re}\Sigma_{A\mu}(0) \approx \rho_{0A}(0)$ and $\mathrm{Im}\Sigma_{A\mu}(0) = 0$. The singularities of $\Sigma_B(z)$ are caused by the NFL peaks in the density of states $\rho_B^{(\pm)}(\varepsilon) - \rho_{0B}(\varepsilon) = \mp 1/\pi A_\rho \mathrm{Im}\mathrm{Sp}\hat{G}_\Lambda^{(\pm)}(\varepsilon)\Gamma\varepsilon \gtrless 0$, $A_\rho \sim \gamma_{\Lambda B}\rho_{0B}$. At zero tem-

perature, the contribution of the resonance level to $\Sigma_{B\mu}(z)$ is proportional to the expression

$$\Sigma_{B\mu}(z) \sim \left(W/z + i\Gamma_K\right)^{1-\alpha_s}(-1)^{\alpha_s - 1}. \qquad (5)$$

The low-lying poles $z_{r\mu}^{(\pm)} = \varepsilon_{r\mu}^{(\pm)} - i\gamma_{r\mu}^{(\pm)}$ of the Green's function $G_{\Lambda\mu}$ are caused by the scattering term H_{sc} and are determined from the equation $D_\mu^{AB}(z_{r\mu}^{(\pm)}) = 0$ (signs $\pm$ correspond to the energies above and below the Fermi level, respectively). One can easily see that this equation has solutions of two types: narrow resonances with $|z_r^{(\pm)}| \ll \Gamma_K$ and "broad" resonances with $|z_r^{(\pm)} + i\Gamma_K| \ll \Gamma_K$. The narrow resonances are of particular interest, because they are responsible for the existence of a small energy scale near the Fermi level. Two types of FL resonances appear because of the existence of the impurity degrees of freedom that are hybridized and nonhybridized with conduction electrons. In particular, the narrow resonances arise as a result of the interband-scattering-induced broadening and shift of the zero-width peak in the NFL spectral function [see the second term in (4)]. The shifts of the narrow resonances from the Fermi level may also be much greater or much smaller than their widths. In the first case ($|\varepsilon_r| \gg \gamma_r$), clearly defined pseudogaps appear in the density of states near the Fermi level (see Fig. 1a). In the second case ($|\varepsilon_r| \ll \gamma_r$), a slightly split narrow resonance occurs at the Fermi level (Fig. 1b). The dashed lines in the figures show the NFL resonances.

The FL resonances can appear on condition that the collective states forming the NFL resonance decay. The binding energy of collective states is of the order of $\varepsilon_K \sim \Gamma_K(W/\Gamma_K)^{\alpha_s}$ and increases with α_s. For this reason, the structure of the FL resonances depends substantially on this parameter. It follows from the solvability condition for the imaginary part of equation $D_\mu^{AB}(z_{r\mu}^{(\pm)}) = 0$ that the narrow resonances near the Fermi level appear at $\alpha_s \leq 3/5$. If $\alpha_s \leq 1/3$, the narrow resonance is split into two components lying above and below the Fermi level. If $\alpha_s > 5/7$, the FL resonances are absent. Power laws occur at $\alpha_s > 1/\ln[\min(\Gamma_K/\gamma_r, W/\Gamma_K)]$.

The narrow resonances also exist at $V_z^\Lambda = 0$. In the strong-coupling limit, the Γ_K value is renormalized to T_K at $h = 0$. In this case, three peaks with the widths $\sim\Gamma_K$, shown in Fig. 1, merge into a single peak that is slightly deformed due to scattering and having the width $\sim T_K$. However, the FL resonances with the width $\sim\gamma_r$ do not disappear (now, $\gamma_r \gg T_K$), because they arise from the scattering of the nonhybridized impurity degrees of freedom.

3. The ratio between the Λ-components $\rho_\Lambda(\varepsilon) = -(1/\pi)\mathrm{Im}\,G_\Lambda(\varepsilon)$ of the partial densities of states at the Fermi level ($\rho_\Lambda(0)$) and at the deep quasilocal level $\rho_\Lambda(\tilde\varepsilon_\Lambda)$, where $\tilde\varepsilon_\Lambda$ is the energy renormalized for
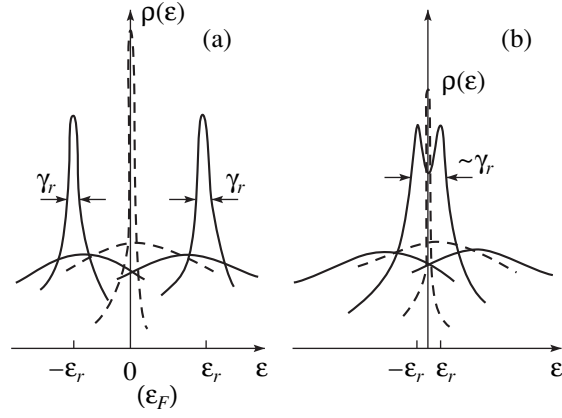

Fig. 1.

hybridization and interaction] serves as a criterion for the discrimination between the mixed- and near-integer-valence HF states. At $\rho_\Lambda(0) \gg \rho_\Lambda(\tilde\varepsilon_\Lambda)$, charged excitations play the dominant role at the Fermi level and ensure the mixed-valent state of the system. The inverse relationship implies that the charge fluctuations are negligible and the system is in the near-integer-valence state.

At energies $|z|$ close to the energy of the deep level, the Green's function $G_\Lambda(z)$ and the maximum value of the density of states can be written as

$$G_\Lambda(z) \approx Z_\Lambda/(z - \tilde\varepsilon_\Lambda), \quad \rho_\Lambda(\tilde\varepsilon_\Lambda) \sim \rho_{0B}(W/\gamma_{\Lambda B}); \quad (6)$$

where Z_Λ is the residue at the pole $z = \tilde\varepsilon_\Lambda = \bar\varepsilon_\Lambda + i\gamma_{\Lambda B}$. Note that, in accordance with the above criterion, one arrives at the well-known exact result [10] that in the case of single-channel Kondo scattering, the density of charged excitation on the Fermi level is negligibly small.

It follows from expressions (3) and (4) that the maximum values of the density of states for the NFL and FL resonances are of the order of magnitude of

$$\rho_\Lambda^{NFL}(0) \sim \rho_{0B}\left(\frac{W}{\Gamma_K}\right)^{1-\alpha_s} \sim \rho_{0B}\left(\frac{\varepsilon_\Lambda}{\gamma_{\Lambda B}}\right)^{2(1-\alpha_s)};$$

$$\rho_{\Lambda B}^{FL}(0) \sim \rho_{0B}\left(\frac{W}{\gamma_r}\right)^{(1-\alpha_s)}. \qquad (7)$$

Comparing (6) with (7), one obtains at $\varepsilon_\Lambda \sim W$

$$\rho_\Lambda^{NFL}(0) \gg \rho_\Lambda(\tilde\varepsilon_\Lambda) \qquad \text{for } \alpha_s < \frac{1}{2};$$

$$\rho_\Lambda^{NFL}(0) \ll \rho_\Lambda(\tilde\varepsilon_\Lambda) \quad \text{for } \alpha_s > \frac{1}{2}, \qquad (8)$$

and the inequalities

$$\rho_\Lambda^{FL}(0) \gg \rho_\Lambda^{NFL}(0), \quad \rho_\Lambda(\tilde\varepsilon_\Lambda). \qquad (9)$$

Inequalities (8) and (9), first, mean that the near-integer-valence state can exist either at $\alpha_s > 1/2$ in the

absence of the FL resonances or at $\alpha_s > 5/7$. The latter condition signifies that the NFL-state instability caused by the presence of FL resonances tangibly narrows the range of existence for the near-integer-valence state. Second, it follows from inequalities (8) and (9) that there are two sorts of mixed-valent states with qualitatively different types of elementary excitations. The mixed-valent NFL state exists at $\alpha_s < 1/2$ and in the absence of FL resonances. The NFL state is of the mixed-valent type, because the collective excitations forming the NFL resonance are charged. The mixed-valent FL state is due to the instability of the NFL state to interband scattering. The conditions imposed on the parameters for its existence are the same as those required for the existence of the FL resonances (i.e., when the inequalities $|z_r^{(\pm)}| \ll \Gamma_K$ and $|z_r^{(\pm)} + i\Gamma_K| \ll \Gamma_K$ are fulfilled). The type of the mixed-valent FL state is determined by the type of the FL resonance (narrow or broad) that occurs at a given parameter set. Since the narrow FL resonances occur over the whole range of existence of the mixed-valent state ($\alpha_s < 1/2$), the mixed-valent FL state exhibits the following features: (1) the occurrence of a small energy scale $\gamma_r \ll \Gamma_K$ and (2) the presence of a pseudogap in the total density of states. The pseudogaps appear between the narrow FL resonances near the Fermi level and the zero-width NFL peak at the Fermi level (Fig. 1a). The pseudogaps are well defined at $|\varepsilon_r| \gg \gamma_r$. The minimum value of the density of states in the pseudogap is equal to the corresponding value for the broad resonance $|z_r + i\Gamma_K| \ll \Gamma_K$. It should be emphasized that the new physical mechanism of formation of a small energy scale near the Fermi level in the mixed-valent state is typical of the unstable-valence impurities (in contrast to the mechanisms considered previously in [4, 11]). Note also that in both limiting cases, $V_x^\Lambda = 0$ and $\tilde{V}_z^\Lambda = 0$, the mixed-valent state exists solely due to the new FL resonances.

The mixed-valent state considered in this work has a local nature, because it is caused by the on-site fluctuations.

Thus, the proposed mechanism allows the unified description of both the NFL behavior generated by the on-site two-channel Kondo scattering and the different types of HF states. The NFL-state instability to interband scattering qualitatively changes the mechanisms of formation of the HF states and results in the appearance of mixed-valent states with elementary excitations of NFL and FL types. It should be particularly emphasized that the commonly discussed role of the spin and charge degrees of freedom in the formation of the HF states in the NFL impurity systems is determined by the value of the α_s parameter, as is demonstrated above. The instability of the NFL state sharply narrows the region dominated by spin fluctuations (i.e., the region of near-integer valence).

Finally, note that the on-site NFL effects can also be substantial in concentrated systems where the concentration c_i of interacting atoms is of the order of unity.

The ground state in such systems is determined by the competition between the intersite interaction, i.e., indirect exchange of the RKKY type for pseudospins and on-site Kondo scattering. The characteristic energies of both interactions in the NFL metals exhibit a power-law dependence on the exchange-interaction constant, but with different exponents. As indicated above, the characteristic energy ε_K of on-site two-channel Kondo scattering is determined as $\varepsilon_K \sim \Gamma_K (W/\Gamma_K)^{\alpha_s}$. The characteristic energy of the RKKY interaction is of the order of $\varepsilon_{RKKY} \sim c_i (V_{ex}^2/W) \sim c_i \Gamma_K$. Comparing these two energies at $c_i \sim 1$, one obtains

$$\begin{aligned} \varepsilon_K \gg \varepsilon_{RKKY} \quad &\text{for} \quad \alpha_s \neq 0, \\ \varepsilon_K \sim \varepsilon_{RKKY} \quad &\text{for} \quad \alpha_s = 0. \end{aligned} \qquad (10)$$

Therefore, the on-site NFL effects can play an important role in the formation of the ground state of concentrated systems at $\alpha_s \neq 0$.

REFERENCES

1. H. V. Löhneysen, Physica B (Amsterdam) **206–207**, 101 (1995).

2. M. B. Maple, R. P. Dickey, J. Herrmann, *et al.*, J. Phys.: Condens. Matter **8**, 9773 (1996).

3. A. Schiller, F. B. Anders, and D. L. Cox, Phys. Rev. Lett. **81**, 3235 (1998).

4. M. Koga and D. L. Cox, Phys. Rev. Lett. **82**, 2575 (1999).

5. D. J. Cox, Phys. Rev. Lett. **59**, 1240 (1987).

6. M. Fabrizio, A. O. Gogolin, and Ph. Nozieres, Phys. Rev. Lett. **74**, 4503 (1995).

7. L. A. Manakova, JETP Lett. **67**, 1069 (1998); L. A. Manakova, Zh. Éksp. Teor. Fiz. **114**, 1466 (1998) [JETP **87**, 796 (1998)].

8. L. A. Manakova, JETP Lett. **69**, 772 (1999).

9. K. A. Kikoin, Physica B **163**, 343 (1990).

10. N. Kawakami and A. Okiji, Phys. Rev. B **42**, 2383 (1990).

11. Yu. Kagan and N. V. Prokof'ev, Zh. Éksp. Teor. Fiz. **93**, 366 (1987) [Sov. Phys. JETP **66**, 211 (1987)].

Translated by R. Tyapaev

====== **CONDENSED MATTER** ======

Current Response of a Superlattice Irradiated with Nonequilibrium Phonons[1]

B. A. Glavin*, V. A. Kochelap, and T. L. Linnik

Institute of Semiconductor Physics, National Academy of Sciences of Ukraine, Kiev, 252028 Ukraine
*e-mail: glavin@class.semicond.kiev.ua
Received February 8, 2000

Abstract—We studied a biased superlattice and revealed a considerable current response to irradiation by nonequilibrium acoustic phonons with an effective temperature on the order of a few Kelvins. We discuss two phonon source–superlattice configurations, for which the current response is caused by either interwell or intrawell electron transitions. We have shown that the response is sensitive to both direction and spectral distribution of phonons. The results explain recent experiments on the phonon-induced current response and prove that the superlattices can be used for the characterization of a high-frequency phonon flux. © *2000 MAIK "Nauka/Interperiodica"*.

PACS numbers: 73.20.Dx; 73.50.-h; 73.61.-r

Semiconductor superlattices (SLs) demonstrate a number of interesting electron-transport phenomena, including Bloch oscillations [1], electron hopping conduction [2, 3], and charge domain formation [4]. It is also established that the electric current in an SL can change substantially under irradiation with electromagnetic waves. In particular, intense THz irradiation of a biased SL can produce extreme effects such as change of the sign of the electric current (absolute negative conductance) [5]. Interest in the effects induced by the irradiation of SLs is stimulated both by the fundamental character of the phenomena and by the possibility of their applications. Among such applications are photodetection [6] and active control of electric currents in devices.

During the last decades, significant progress has been achieved in the development of the methods of phonon detection, generation, and control [7]. This makes it possible to irradiate different quantum heterostructures by phonon fluxes and study the effects induced by such an irradiation [8]. The first experimental observation of a current response (CR) of a phonon-irradiated SL was reported [9]. In this letter, we analyze the basic mechanisms of CR to the acoustic phonon flux. Our results explain the main features observed in [9] and demonstrate that the CR provides valuable information on the phonons; i.e., it can be used for phonon flux characterization. The results also show the way to control electric current by phonons.

For the hopping transport regime [2, 3], there are two basic mechanisms through which the acoustic phonons affect the SL current. First, the phonons make a direct contribution to the current by initiating *inter-*

well electron transitions. Second, the nonequilibrium phonons induce *intrawell electron transitions* resulting in electron heating and, thus, indirectly change the electric current. It is important that both mechanisms result in qualitatively different types of CR and, hence, can easily be discriminated in the experiment.

The scheme of the system under consideration is shown in Fig. 1. The semiconductor structure is similar to that used in [9]. The SL is situated on the top of a substrate of thickness L_s. The sources of nonequilibrium phonons are on the opposite side of the substrate. As a rule, the phonons are generated by thin metallic films. When heated to temperature T_f by a short laser pulse or electric current pulse, the metallic film emits acoustic phonons into the substrate. The emitted phonons can be characterized by the Planck distribution with temperature T_f that exceeds the substrate tem-
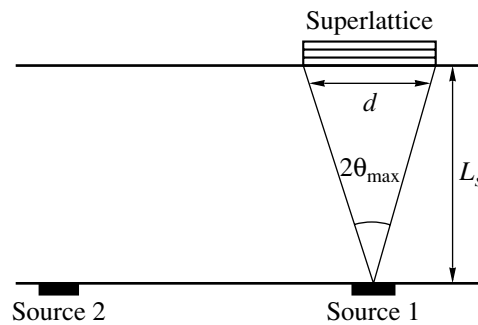

Fig. 1. Scheme of the system under consideration. The biased SL is irradiated with nonequilibrium phonons generated by the phonon sources. The two sources shown in the figure produce qualitatively different electron transitions and CRs.

---

[1] This article was submitted by the authors in English.

perature T. At low temperatures T_f and T, the mean free path of almost all emitted phonons is greater than the typical substrate thickness $L_s \sim 300$–500 μm. Because of this, the phonons propagate from the source through both substrate and SL almost ballistically. In the SL, the phonons induce electron transitions and cause changes in the current.

In the III–V-SLs, the acoustic mismatch is relatively small and only brings about the modification of the phonon spectra (phonon folding). These modifications are significant only near the boundary and the center of the superlattice Brillouin zone, while the nonequilibrium phonons generated by a heat pulse have a relatively broad distribution in **q**. Thus, for our purposes, we can treat the nonequilibrium phonons within the framework of the bulk model and characterize them by the wave vector **q**. Let θ be the angle between **q** and the SL axis. Since the SL width L_w and thickness D, as well as the source dimensions, are usually much smaller than the substrate thickness, the ballistic phonons incident on the SL have a very narrow distribution in θ. The characteristic θ value is determined by the position of the phonon source relative to the SL. In Fig. 1, we show schematically two different source–superlattice configurations. Source 1 is placed exactly under the SL. In this case, the phonons reaching the SL have small θ values, $\theta < \theta_{max} \approx L_w/(2L_s)$. In contrast, source 2 is situated clear of the SL, so that the phonons of interest have $\theta \approx \pi/2$. It is shown below that these two sorts of phonons with $\theta \ll \pi/2$ and $\theta \sim \pi/2$ have qualitatively different effects on the electron transitions and bring about distinct CRs. The experimental setup in [9] was similar to the source–superlattice configuration I.

We restrict ourselves to the consideration of the SL in the hopping conduction regime caused by the electron transitions between the neighboring QWs [2, 3]. This occurs when the Stark splitting Δ is larger than the SL miniband width. The electronic states form the Stark ladder spectrum

$$E_{n,k} = \hbar^2 k^2/2m - n\Delta + E_0, \qquad (1)$$

where k is the in-plane wave vector, n is the number of a quantum well, and E_0 is the energy reference. For the electron wave functions, we use the so-called two-well model described, e.g., in [2, 10]:

$$\Psi_{n,k} = \frac{1}{\sqrt{S}}\exp(i\mathbf{k}\boldsymbol{\rho})\psi_n(z), \qquad (2)$$

$$\psi_n = \chi(z - nd)$$

$$-\frac{t}{\Delta}(\chi(z - (n+1)d) - \chi(z - (n-1)d)).$$

Here, $\boldsymbol{\rho} = (x, y)$ is the in-plane electron coordinate, z-direction is parallel to the SL axis, S is the normalization area of the QW layer, χ is the normalized wave function in the individual QW, and t is the overlap inte-

gral $t = V_0\int\chi(z - nd)\chi(z - (n+1)d)dz$. Wave functions (2) describe the Stark ladder states under the condition $t \ll \Delta \ll V_0$, where V_0 is the barrier height. We assume that the electron–phonon interaction arises from the deformation potential and use the standard Hamiltonian for this interaction [11, 12].

The intrawell transitions occur between the electronic states within the same QW, $\{n, k\} \longleftrightarrow \{n, k'\}$, while the interwell transitions occur between the electronic states of the neighboring QWs, $\{n, k\} \longleftrightarrow \{n \pm 1, k'\}$. One can easily see that, due to the energy and momentum conservation laws, the intrawell phonon-assisted transitions occur mainly for the phonons with $\theta > s/v_F$, where s is the sound velocity and v_F is the Fermi electron velocity. Therefore, if the geometry of the system satisfies the condition $(L_w/2L_s) \leq (s/v_F)$ for the source–superlattice configuration I, the phonons mainly induce the interwell transitions. In this case, the CR can be written as the sum of contributions from different interwell processes:

$$\Delta J^I = \frac{e}{S}\sum_{\mathbf{q}}(P_{em}^{(down)} + P_{ab}^{(down)} - P_{em}^{(up)} - P_{ab}^{(up)})N_q$$

$$\equiv \Delta J_{em}^{(down)} + \Delta J_{ab}^{(down)} - \Delta J_{em}^{(up)} - \Delta j_{ab}^{(up)}, \qquad (3)$$

where $P(q)$ are the probabilities of phonon emission or absorption accompanied by the electron transfer "up" or "down" the Stark ladder and N_q are the occupation numbers of the nonequilibrium phonons. Expressions for P have the form

$$P_{(em,ab)}^{(down,up)}(q) = \frac{2\pi}{\hbar}|M(n, n'|q_z)|^2$$

$$\times \sum_{k,k'}\delta_{\mathbf{k}\mp\mathbf{q}_{\parallel},k'}\delta[E_{n,k} - E_{n',k'} \mp \hbar\omega]\mathscr{F}_{n,k}[1 - \mathscr{F}_{n',k'}], \qquad (4)$$

where $M(n, n'|q_z)$ is the matrix element calculated with the wave functions $\psi_n, \psi_{n'}$; $\mathbf{q}_{\parallel}$ is the in-plane projection of **q**; and $\mathscr{F}_{n,k}$ is the Fermi distribution function for electrons in the $n^{th} - QW$, where the upper signs stand for the emission and the lower signs stand for the absorption processes. The "down" and "up" transitions correspond to $n' = n \pm 1$, respectively. The intrawell transitions can be evaluated in a similar manner.

Below, we discuss CR (3) for the SL with the following parameters. The quantum-well and barrier-layer thicknesses are taken to be 4.5 nm and 6 nm respectively; $L_w = 100$ μm; and $L_s = 500$ μm. The electron effective mass is $m = 0.067m_0$, and the barrier height $V_0 = 1$ eV, providing the SL miniband width of 0.1 meV. The electron density is $n_e = 2 \times 10^{14}$ m^{-2}. To describe the phonons interacting with electrons, we set the longitudinal sound velocity $s_l = 4800$ m/s and material density $\rho = 5300$ kg/m^3. The deformation potential con-

stant is taken to be $E_1 = 7$ eV. We also performed calculations for hopping transport in a GaAs/AlGaAs superlattice with different parameters and arrived at results similar to those discussed below.

Figure 2 shows the partial contributions to the CR as functions of the Stark splitting Δ for the source–SL configuration I. The source temperature is 5 K. The results correspond to the zero-temperature limit for the SL.

The dependences obtained can be qualitatively explained as follows. As seen from (2), the interwell matrix element $|M(n, n \pm 1|q)|$ decreases when Δ increases (see also [2, 10]). The energy and momentum conservation laws impose limitations on the possible electronic states involved in the transitions. Combining these limitations with the Fermi distribution at $T \longrightarrow 0$, we find that the up-transitions are entirely forbidden for the phonon emission ($\Delta J_{em}^{(up)} = 0$), while the up-transitions with phonon absorption are allowed for the phonon energy $\hbar\omega > \Delta$. The down-processes with phonon absorption are allowed for any phonons. This explains the monotonic decrease in functions $\Delta J_{ab}^{(up)}$ and $\Delta J_{ab}^{(down)}$. The down-transitions with phonon emission are allowed at $\hbar\omega < \Delta$. This limitation on the number of phonons participating in the down-transitions results in a decrease in $\Delta J_{em}^{(down)}$ at small Δ: the function $\Delta J_{em}^{(down)}(\Delta)$ becomes nonmonotonic.

The net CR as a function of the Stark splitting is shown in Fig. 3. Two remarkable features of the CR are seen in this figure. First, the CR can have both negative and positive signs. At low Δ values, the CR is negative, because the up-absorption processes dominate and, hence, phonons drive electrons up the Stark stairs. The negative CR means that the phonons partially suppress the SL current. The suppression effect increases with decreasing Δ. This is quite similar to the effect observed at THz electromagnetic irradiation [5]. At higher Δ, the down-emission processes prevail and the CR becomes positive.

The second feature is that the CR is a nonmonotonic function of Δ. The maximum value of ΔJ^I increases with an increase in the temperature T_f of the phonon source and occurs at larger Δ. The nonmonotonic behavior of CR at fixed T_f, the increase in the maximum response, and its shift at higher T_f were observed in experiments [9]

The above results were obtained for the phonon source–superlattice configuration I, when the intrawell phonon processes are excluded and electron heating does not occur. The insert in Fig. 3 demonstrates the change in the SL current $\Delta J^{II} \equiv J(T_e) - J(0)$ caused by electron heating. The shape of the function $\Delta J^{II}(\Delta)$ and its sign and magnitude are radically different from those of ΔJ^I. Thus, one should expect a different char-
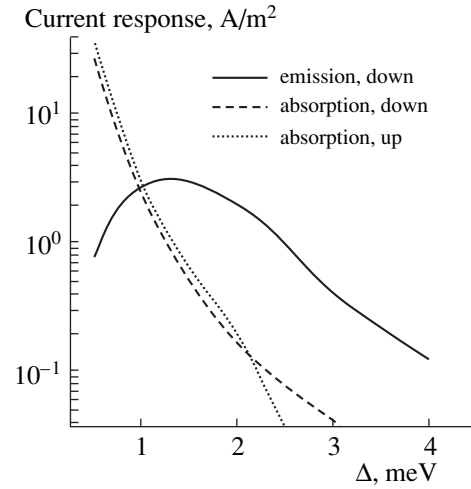

Fig. 2. Partial contributions to the CR as functions of Stark splitting Δ for the photon source temperature $T_f = 5$ K.
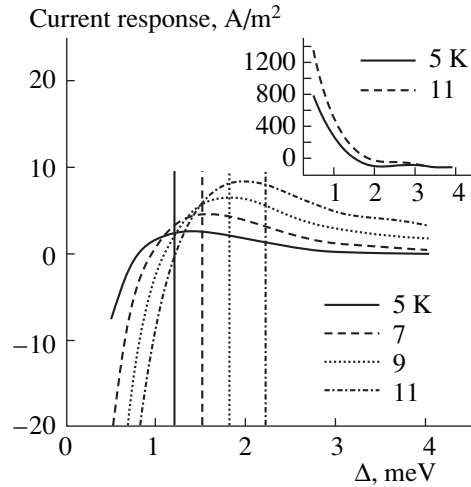

Fig. 3. CR caused by the interwell electron transitions as a function of Stark splitting for several temperatures of the photon source. The vertical lines correspond to the critical Stark splittings Δ_c. Insert: change ΔJ^{II} in the current caused by electron heating for different electron temperatures T_e.

acter of the CR for the source–superlattice configuration II, when the intrawell transitions mostly occur. On the other hand, a comparison of ΔJ^I and ΔJ^{II} proves that, in the experiments [9], the interwell phonon-induced transitions were observed. Note that we used the isotropic elastic model for the crystal, which provides the electron–phonon coupling with LA phonons only. However, the crystal anisotropy and the LA–TA mixing in the SLs can lead to a nonzero CR for the TA phonons as well, as was indeed detected in [9].

One more interesting conclusion can be drawn from the calculations of the partial contributions to the CR shown in Fig. 2. Let Δ_c be a solution to the equation

$\Delta J_{em}^{(down)}(\Delta) = \Delta J_{ab}^{(up)}(\Delta) + \Delta J_{ab}^{(down)}(\Delta)$. Then at $\Delta > \Delta_c$ the rate of stimulated emission exceeds the total rate of all absorption processes. This, in fact, corresponds to the *amplification* of the phonon flux in the SL. This is in agreement with the results [13], where we showed that the phonons with energies below Δ are amplified in the case of hopping transport in a biased SL. The values of $\Delta_c(T_f)$ are shown in Fig. 3. We see that, indeed, $\Delta_c(T_f) > k_B T_f$; i.e., almost all propagating phonons are amplified by the SL current.

In conclusion, we studied the irradiation of SL by nonequilibrium phonons and calculated the CR. We analyzed different mechanisms of phonon-induced electron transfer contributing to the CR. We showed that the character of CR is highly sensitive to the phonon source–superlattice configuration, as well as to the phonon temperature. This sensitivity allows one to use the CR for detecting and characterizing the phonon fluxes. For the average phonon energy smaller than the Stark splitting we found that the stimulated emission processes dominate over the processes with absorption; i.e., the phonon flux can be amplified upon propagation through the SL.

ACKNOWLEDGMENTS

REFERENCES

1. F. Agullo-Rueda and J. Feldmann, in *Semiconductor Superlattices*, Ed. by H. T. Grahn (World Scientific, Singapore, 1995).
2. R. Tsu and G. Döhler, Phys. Rev. B **12**, 680 (1975).
3. A. Wacker and A.-P. Jauho, Phys. Rev. Lett. **80**, 369 (1998).
4. H. Grahn, in *Semiconductor Superlattices*, Ed. by H. T. Grahn (World Scientific, Singapore, 1995).
5. B. J. Keay, S. Zeuner, S. J. Allen, *et al.*, Phys. Rev. Lett. **75**, 4102 (1995).
6. A. A. Ignatov and A.-P. Jauho, J. Appl. Phys. **85**, 3643 (1999) and references therein.
7. *Proceedings of the International Conference Phonons-98*, Physica B (Amsterdam) **263–264** (1999).
8. D. N. Hill, S. A. Cavill, A. V. Akimov, *et al.*, Phys. Status Solidi B **204**, 431 (1997).
9. S. A. Cavill, A. V. Akimov, F. F. Ouali, *et al.*, Physica B (Amsterdam) **263–264**, 537 (1999).
10. F. T. Vasko, Fiz. Tekh. Poluprovodn. (St. Petersburg) **26**, 825 (1992) [Sov. Phys. Semicond. **26**, 464 (1992)].
11. V. E. Gantmakher and Y. B. Levinson, *Carrier Scattering in Metals and Semiconductors* (North-Holland, Amsterdam, 1987).
12. V. V. Mitin, V. A. Kochelap, and M. A. Stroscio, *Quantum Heterostructures* (Cambridge Univ. Press, Cambridge, 1999).
13. B. A. Glavin, V. A. Kochelap, and T. L. Linnik, Appl. Phys. Lett. **74**, 3525 (1999).

<center>= CONDENSED MATTER =</center>

Multilayer Composite Epitaxial CuCo Single Crystals

É. S. Mushailov[1], P. D. Kim[1,]*, I. A. Turpanov[1], G. V. Bondarenko[1],
G. N. Bondarenko[2], and S. É. Mishina[3]

[1]*Kirenskiĭ Institute of Physics, Siberian Division, Russian Academy of Sciences,*
Akademgorodok, Krasnoyarsk, 660036 Russia
[2]*Institute of Chemistry and Chemical Technology, Siberian Division, Russian Academy of Sciences, Krasnoyarsk, Russia*
[3]*Krasnoyarsk State University, Krasnoyarsk, 660049 Russia*
*e-mail: kimpost@krascience.rssi.ru
Received February 1, 2000

Abstract—The ion-plasma spraying method was used to synthesize new phases of metastable atomic-ordered layered CuCo single crystals and single crystals of Cu_cCo_{1-c} solid solutions via epitaxial layer-by-layer crystallization, and some of their physical properties were studied. © *2000 MAIK "Nauka/Interperiodica".*

PACS numbers: 68.65.+g; 75.70.-i; 81.15.Rs

The study of layered compositionally modulated crystal structures exhibiting promising solid-state properties is one of the "hot" areas of physical metallurgy. The nature of magnetic ordering and the giant magnetoresistance of the artificial periodic superlattices comprised of alternating magnetic and nonmagnetic layers generate considerable interest among researchers. At present, it is generally believed that the transition-metal layers in multilayer systems are magnetically ordered, while the interlayer exchange interactions, e.g., of the RKKY type, can only result in oscillations of the ferro- or antiferromagnetic ordering, depending on the thickness of the nonmagnetic layers [1, 2]; i.e., the multilayer effect on the intralayer exchange interactions is *a priori* ignored. The experimental results obtained in our work [3, 4] allow one to suggest a somewhat different point of view on the nature of magnetic ordering, at least in multilayer monatomic polycrystalline $(Cu/Co)_x$ structures.

Unexpected results were obtained when we synthesized artificial epitaxial composite multilayer $(Cu/Co)_x$ crystal superlattices to continue our experiment. The crystal structures revealed the cooperative atomic ordering phenomenon.

Single-crystal multilayer film structures $(n_1Cu/n_2Co)_x$, where n_1, n_2, and x are the number of monatomic Cu layers, the same for Co, and the number of bilayers, respectively, were grown via the epitaxial technique through layer-by-layer crystallization on the MgO and LiF (001) crystal surfaces obtained by cleaving bulky single crystals along the atomic cleavage planes. The ion-plasma spraying technique was applied to deposit metals on supports heated to the epitaxial temperatures.

The results of the X-ray structural and magnetic studies carried out in this work can be generalized by the following epitaxial relation between the MgO, LiF, Cu, and Co crystal lattices:

$$FCCMgO(001)[001]\|\{FCCn_1Cu(001)[001]\| \times FCCn_2Co(001)[001]\}_x, \quad (1)$$

$$FCCLiF(001)[001]\|\{FCCn_1Cu(001)[001]\| \times FCCn_2Co(001)[001]\}_x. \quad (2)$$

X-ray structural studies were performed by X-ray diffractometry on a DRON-4 spectrometer at room temperature with CuK_α radiation.
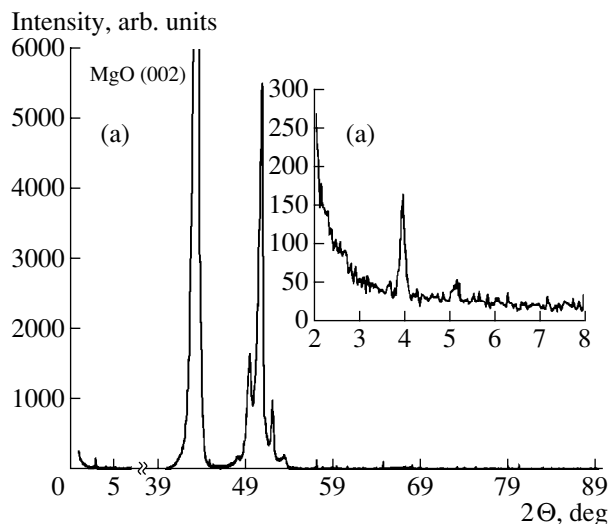

Fig. 1. X-ray pattern of a multilayer [Cu(36 Å)/Co(38 Å)]$_{30}$ single crystal (CuK_α, room temperature): (a) is the small-angle scattering region, and MgO(002) indicates the reflection from a single-crystal support.
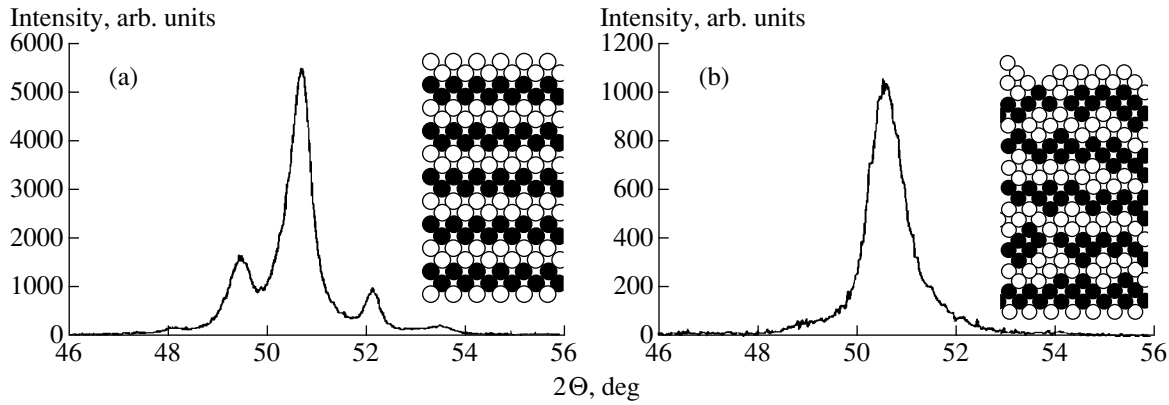
Fig. 2. Portions of the X-ray patterns of two multilayer single-crystal samples (CuK_α, room temperature, large-angle scattering region): (a) [Cu(36 Å)/Co(38 Å)]$_{30}$ and (b) [Cu(28 Å)/Co(25 Å)]$_{30}$. The interfaces between the layers (fragments of computer simulation) are schematically represented in the insets illustrating the distinctions in X-ray diffraction.

The superstructure composition modulation periods were determined from the superstructure diffraction reflections for the small (small-angle scattering) and large (large-angle scattering) X-ray scattering vectors, as well as by the X-ray fluorescence method. The positions of diffraction peaks in the X-ray patterns fit the following relationships.

Small-angle scattering:

$$\sin\Theta = \frac{\lambda_0}{2\Lambda}N \quad \text{(principal maxima),} \tag{3}$$

$$\sin\Theta = \frac{\lambda_0}{2\Lambda}\left(N + \frac{2n+1}{x}\right) \quad \text{(subsidiary maxima),} \tag{4}$$

where λ_0 is the radiation wavelength, Θ is the Bragg angle, Λ is the superlattice spacing, and N and n are the reflection periods.

Large-angle scattering:

$$\sin\Theta = \frac{\lambda_0}{2d}N \quad \text{(central maximum),} \tag{5}$$
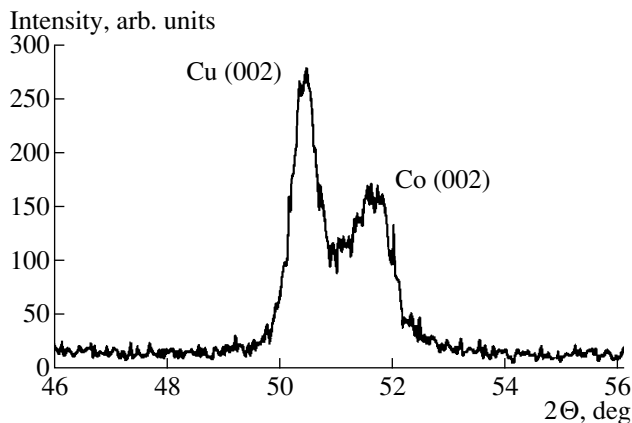

Fig. 3. X-ray diffraction spectrum of a two-layer composite single crystal Cu(680 Å)/Co(580 Å).

$$\sin\Theta = \frac{\lambda_0}{2}\left(\frac{N}{d} \pm \frac{k}{\Lambda}\right)$$
$$\text{(satellites of the central maximum),} \tag{6}$$

$$\sin\Theta = \frac{\lambda_0}{2}\left(\frac{N}{d} \pm \frac{2n+1}{\Lambda x}\right) \quad \text{(subsidiary maxima),} \tag{7}$$

where d is the mean interplanar spacing and k is the order of reflection.

It is customarily believed (theory and experiment) [5–7] that the position of the central peak in the X-ray patterns of the multilayer superstructures corresponds to the mean d value (weighted mean of the number of individual lattice planes). This rule is violated for the structures considered in this work. The position of the central peak corresponds to the interplanar spacing d_{002} in a pure copper single crystal (Figs. 2, 3). This and other results of our X-ray measurements, as well as the results of the magnetic, galvanomagnetic, electrical, and thermal studies allow the following conclusion to be drawn. The layered atomic-ordered single-crystal CuCo structures, metastable at room temperature (on vacuum heating to 800°C, the metastable phase converts into a stable two-phase structure representing a mixture of pure copper and cobalt phases, in accordance with the phase diagram for the cobalt–copper alloy), were grown by the epitaxial technique. We associate the metastability of the close-packed FCC crystal structure of CuCo with a peculiar (excited) electronic state of the Co atoms, which is experimentally manifested as an increase in the metallic radius of 2%.

We also synthesized and studied the structures with atomic disorder (single crystals of solid solutions). Such structures can be prepared by the epitaxial layer-by-layer crystallization of alternating Cu and Co layers with effective thicknesses of less than one monatomic layer. The concentrations of components in the alloy are experimentally predetermined by the ratio of effective thicknesses. According to the phase diagram of a cobalt–copper alloy prepared by cooling (including

superfast cooling [8]) liquid solutions, the solid solutions synthesized in our work cannot exist. Similar to the layered single crystals described above, the metallic radius of Co in the single crystals of CuCo solid solutions is 2% larger than in a pure cobalt phase. The solid solution is thermodynamically unstable (metastable). On vacuum heating, the solid solution is layered into pure Co FCC and Cu FCC phases.

Single crystals of intermediate structures were also prepared and studied. They can be regarded as partially disordered layered single crystals or partially ordered solid solutions. The physical properties of such structures are widely diversified and can even be quite unusual.

The general regularity (sequence) of the structural transformations during the heating ⟷ cooling thermal cycle (with the retention of the close-packed single-crystal FCC structure) is as follows: the metastable structure with atomic disorder ($Cu_c Co_{1-c}$ solid solution) ⟶ metastable atomic-ordered structure [layered $(Cu/Co)_x$ single crystal] ⟶ two-phase stable structure (composite single-crystal Co + Cu).

The layered single crystals are ferromagnetic with cubic magnetocrystalline anisotropy in the (001) plane. For the cobalt layers of thickness 15 Å and over, the saturation magnetization I_s and the first magnetocrystalline anisotropy constant K_1 are close to the analogous values for a pure cobalt FCC single crystal (per the same cobalt amount in the CuCo structure). For cobalt layers of thickness less than 15 Å, the ferromagnetic ordering depends on the thickness of the copper layer [3].

The room-temperature transverse magnetoresistance anisotropy $d\rho/\rho dH$ is positive for the layered CuCo FCC single crystals, whereas the anisotropy of the Co FCC single crystal has negative sign.

Single crystals of the $Cu_c Co_{1-c}$ solid solutions are ferromagnetically ordered and magnetically anisotropic over a wide range of copper concentrations c. The saturation magnetization I_s is a linear function of copper concentration. The atomic magnetic moment μ changes as

$$d\mu/\mu_b dc = 2; \qquad (8)$$

i.e., the $Cu_{0.86} Co_{0.14}$ alloy is nonmagnetic at any temperature [expression (8) was obtained by extrapolating the experimentally measured dependence of the room-temperature saturation magnetization I_s on the copper concentration c to the temperature $T = 0$]. The experimental result (8) agrees well with the theoretical model of two "hard" bands, one of which is only partially filled [9].

The magnetocrystalline cubic anisotropy in the (001) plane depends on the copper concentration, in accordance with the relation $K_1 \simeq I_s^2$. The results obtained in this work for the $Cu_c Co_{1-c}$ alloys are similar to those previously obtained for the $Cu_c Ni_{1-c}$ alloys exhibiting infinite mutual solubility [10].

We plan to systematically study the synthesized new materials in future works.

REFERENCES

1. J. J. de Miguel, A. Cebollada, J. M. Gallego, *et al.*, J. Magn. Magn. Mater. **93**, 1 (1991).

2. J. L. Martínez, A. Cebollada, J. M. Gallego, *et al.*, J. Magn. Magn. Mater. **93**, 89 (1991).

3. E. S. Mushailov, V. K. Maltsev, I. A. Turpanov, and P. D. Kim, J. Magn. Magn. Mater. **138**, 207 (1994).

4. P. D. Kim, I. A. Turpanov, V. K. Maltsev, *et al.*, Pis'ma Zh. Éksp. Teor. Fiz. **64**, 341 (1996) [JETP Lett. **64**, 370 (1996)].

5. K. E. Meyer, G. P. Felcher, S. K. Sinha, *et al.*, Appl. Phys. **52**, 6608 (1981).

6. J. K. Schuller, Phys. Rev. Lett. **44**, 1597 (1980).

7. E. E. Fullerton, J. K. Schuller, and H. Vanderstraen, Phys. Rev. B **45**, 9292 (1992).

8. T. R. Anantharaman and C. Suryanarayana, J. Mater. Sci. **6**, 111 (1971).

9. S. V. Vonsovskiĭ, *Magnetism* (Nauka, Moscow, 1971).

10. R. M. Bozorth, *Ferromagnetism* (Van Nostrand, New York, 1951; Inostrannaya Literaturas, Moscow, 1956).

Translated by V. Sakun

<div align="center">

CONDENSED MATTER

</div>

Linear Dynamics of a Magnetic Subsystem in a Quasi-Ising Magnet

A. S. Lagutin and G. E. Fedorov*

Institute of Molecular Physics, Russian Research Centre Kurchatov Institute,
pl. Kurchatova 1, Moscow, 123182 Russia
*e-mail: fedorov@imp.kiae.ru
Received February 2, 2000

Abstract—Microwave absorption at frequencies from 37 to 85 GHz was studied for a $Dy_{0.3}Y_{2.7}Fe_5O_{12}$ single crystal in pulsed magnetic fields of up to 30 T at $T = 4.2$ K. The magnetic field was aligned with the [100] direction. For the fields above 4 T, several soft magnetic-resonance modes were observed, most of them being caused by the static phase transitions induced by a strong external magnetic field. The field-independent absorption lines away from the points of phase transition may be due to the dynamic Jahn–Teller magnetic effect. © 2000 MAIK "Nauka/Interperiodica".

PACS numbers: 75.50.Gg; 76.30.-v; 75.30.Kz

Recent experimental studies of the static magnetic properties (magnetization and differential magnetic susceptibility) of mixed garnet ferrites $Dy_xY_{3-x}Fe_5O_{12}$ have shown that the low-temperature rearrangement of their magnetic structures in strong magnetic fields is accompanied by sharp magnetic-moment jumps, with the jump magnitude and number depending on the orientation of the external magnetic field about the crystallographic axes [1, 2]. The theoretical analysis of the magnetic-field-induced phase transitions in $Dy_xY_{3-x}Fe_5O_{12}$ suggested [3] that satisfactory agreement between the experiment and theory can be achieved if one assumes that there is a quasi-Ising ordering of the Dy^{3+} ions. This implies that at low temperatures the RE-ion ground state can be regarded as an isolated doublet ($S_{eff} = 1/2$) with strongly anisotropic g tensor [3, 4]. Within the framework of a phenomenological model, the presence of several nonzero components of this tensor allows not only 180° rotations of the RE magnetic moments, as in the pure Ising model [5], but also the rotation of these moments toward the external-field direction.

The detailed low-temperature magnetic-resonance studies of $Ho_xY_{3-x}Fe_5O_{12}$ single crystals in strong magnetic fields [6] provide evidence for the occurrence of a magnetic analogue not only of the static but also of the dynamic Jahn–Teller effect in these compounds. The latter manifests itself in the soft magnetic-resonance modes appearing away from the magnetostructural phase-transition points, i.e., in the region where the RE ground state remains unchanged.

Inasmuch as the $Ho_xY_{3-x}Fe_5O_{12}$ system is the only one for which the magnetic analogue of the dynamic Jahn–Teller effect has been observed to date, a search for other crystals exhibiting analogous resonance char-

acteristics is very important and of interest for studying the properties of this phenomenon. In this work, mixed dysprosium garnet ferrites were chosen as the object of investigation because their magnetization curves resemble those for $Ho_xY_{3-x}Fe_5O_{12}$ (in both cases, the sharp magnetic-moment jumps are observed, with the jump magnitude and number depending on the orientation of the external magnetic field) and their ground state at low temperatures can also be considered as a quasi-doublet with strongly anisotropic g tensor [7, 8].

This work reports the results of studying microwave absorption for a $Dy_{0.3}Y_{2.7}Fe_5O_{12}$ single crystal in the frequency range from 37 to 85 GHz and magnetic fields of up to 30 T at temperature 4.2 K. One of the samples whose static magnetic characteristics were
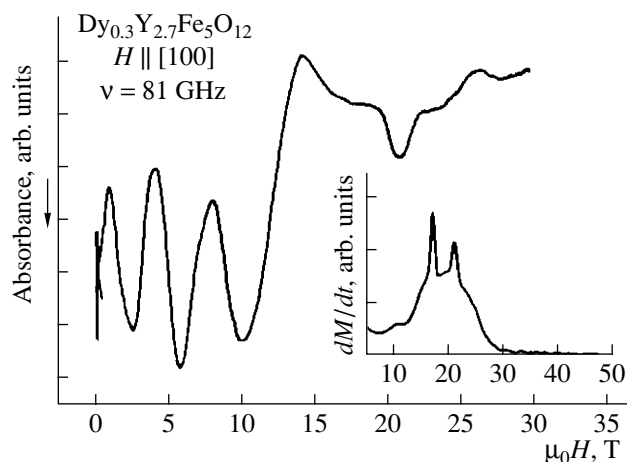

Fig. 1. Absorption signal recorded for a $Dy_{0.3}Y_{2.7}Fe_5O_{12}$ single crystal at $T = 4.2$ K and $H \parallel$ [100]. Field-dependent dM/dt is shown for the same sample in the inset.

examined earlier in [1] was used in the experiments. The external magnetic field was aligned with the crystal [100] axis, and all measurements were made with a reflection-type radiospectrometer whose construction was described in [9].

The analog signal from the detector is fed into a B3-57 preamplifier and then to one of the channels of a DF1200 digital single-event recorder, whose second channel was used for recording voltage proportional to the external magnetic field. Magnetic-resonance studies were carried out at fixed frequencies with magnetic-field sweep.

A typical absorption spectrum of a $Dy_{0.3}Y_{2.7}Fe_5O_{12}$ crystal is shown in Fig. 1. One can identify several magnetic-resonance branches over the whole range of external fields used. The inset in Fig. 1 demonstrates the field-dependent differential magnetic susceptibility (dM/dt) of the sample studied. A comparison of the absorption curve in Fig. 1 with the dM/dt curve allows some of these resonances to be straightforwardly related to the static magnetic phase transitions in the $H_1 < H < H_2$ range, where the RE ions undergo magnetization reversal [3]. In this region, $H_{2,1} = H_{ex}(1 \pm M_R/M_{Fe})$, where $H_{ex} = 21$ T [1] is the exchange field between the RE and iron subsystems and M_R and M_{Fe} are their magnetizations. It is shown in [5] that such transitions in RE garnet ferrites can be treated as manifestations of a magnetic analogue of the static Jahn–Teller effect, which is caused by the field-induced degeneracy of the ground state of the RE subsystem.

The evolution of absorption lines with changing microwave frequency in the $H_1 < H < H_2$ region is shown in Fig. 2. An unusual magnetic-resonance feature, namely, the presence of absorption at all frequencies at a fixed field (soft mode) is typical of all microwave lines in this magnetic-field range, but is most pronounced and clearly defined for the most intense line (indicated by arrow in Fig. 2).

For each of the microwave frequencies, the absorption spectrum was processed in such a way that the magnetic fields corresponding to the absorption maxima were treated as magnetic-resonance fields. The resonance frequencies thus obtained are plotted in Fig. 3 as functions of the external magnetic field. One can distinguish several well-separated lines (differently marked in Fig. 3) in the range of fields used. For instance, four resonance branches with linearly field-dependent frequencies are observed at weak fields below 5 T (open squares and circles in Fig. 3), with only one of them (open circles) converging to $\nu = 0$ on the extrapolation to $H = 0$. This branch is precisely the one which can logically be assigned to ferromagnetic resonance, because the corresponding $\gamma = 2\pi\nu/H$ value is close to the value found for both yttrium iron garnet and mixed garnet ferrites at the same temperature [10, 11]. The other resonance branches with linearly dependent frequencies (open squares in Fig. 3) correspond to the dimensional resonances.
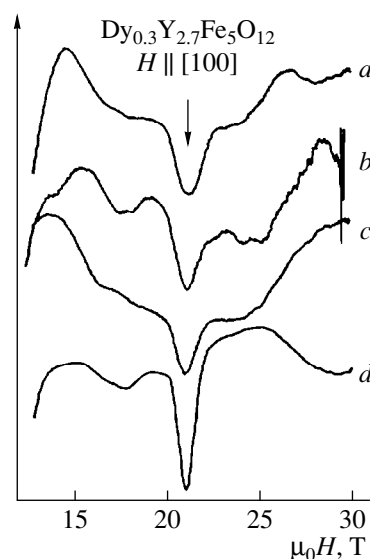
Fig. 2. Frequency-dependent magnetic-resonance lines recorded for a $Dy_{0.3}Y_{2.7}Fe_5O_{12}$ single crystal at $T = 4.2$ K and $H \parallel [100]$: (a) 81, (b) 66.9, (c) 51.62, and (d) 41.16 GHz.

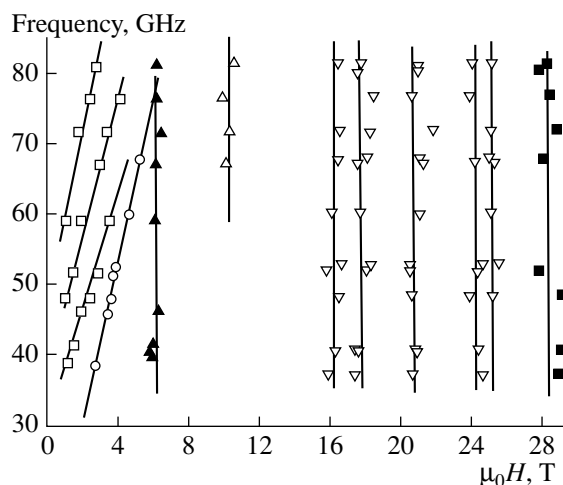**Fig. 3.** Magnetic-resonance pattern for $Dy_{0.3}Y_{2.7}Fe_5O_{12}$ at $T = 4.2$ K and $H \parallel [100]$: □ are for the dimensional resonances; ▽ are for the soft modes in the magnetization reversal region of the rare-earth subsystem; △ are for the resonance corresponding to the magnetic transition at $H = 10$ T; ▲ are for the soft magnetic-resonance modes not associated with the magnetization reversal of the rare-earth subsystem; and ■ are for the ferromagnetic resonance line.

As was expected, the soft magnetic-resonance modes exist in $Dy_{0.3}Y_{2.7}Fe_5O_{12}$ not only at $H_1 < H < H_2$ ($14 < H < 25$ T) but also away from this region, much as it was previously observed for $Ho_xY_{3-x}Fe_5O_{12}$ [6]. Only one of them (at $H = 10$ T) can be related to a magnetic anomaly that is not associated with the reorientation of the RE moments [3]. As to the two other characteristic absorption lines (dark squares and triangles in Fig. 3), they are observed at the fields where the mag-

netic susceptibility does not show any changes (see inset in Fig. 1).

In our opinion, it is precisely these resonances which can be assigned to the manifestations of a magnetic analogue of the dynamic Jahn–Teller effect that were observed previously only for yttrium holmium garnet ferrites [6]. Nevertheless, the ultimate conclusion about the existence of this phenomenon in yttrium dysprosium garnet ferrites can be drawn only after studying the dynamic magnetic phase diagrams of $Dy_{0.3}Y_{2.7}Fe_5O_{12}$ in the "field–temperature" plane and after comparing the results of these studies with the static magnetic data. We are planning to implement this program in the near future.

REFERENCES

1. A. S. Lagutin, G. E. Fedorov, A. V. Kopylov, *et al.*, JETP Lett. **67**, 584 (1997).

2. A. S. Lagutin, G. E. Fedorov, A. V. Kopylov, *et al.*, Physica B (Amsterdam) **246–247**, 520 (1998).

3. A. S. Lagutin, G. E. Fedorov, J. Vanacken, and F. Herlach, J. Magn. Magn. Mater. **195**, 97 (1999).

4. G. A. Babushkin, V. A. Borodin, V. D. Doroshev, *et al.*, Zh. Éksp. Teor. Fiz. **87**, 989 (1984) [Sov. Phys. JETP **60**, 564 (1984)].

5. A. K. Zvezdin, V. M. Matveev, A. A. Mukhin, and A. I. Popov, *Rare-Earth Ions in Magnetically Ordered Crystals* (Nauka, Moscow, 1985).

6. A. S. Lagutin, Sov. Phys. JETP **75**, 138 (1992).

7. R. Z. Levitin and V. I. Silant'ev, Izv. Akad. Nauk SSSR, Ser. Fiz. **44**, 1433 (1980).

8. V. I. Silant'ev, A. I. Popov, R. Z. Levitin, and A. K. Zvezdin, Zh. Éksp. Teor. Fiz. **78**, 640 (1980) [Sov. Phys. JETP **51**, 323 (1980)].

9. A. S. Lagutin, in *Proceedings of the International Workshop on Research in High Pulsed Magnetic Fields, Toulouse, France, 1993*, p. J3-1.

10. A. G. Gurevich, *Magnetic Resonance in Ferrites and Antiferrites* (Nauka, Moscow, 1973).

11. S. Krupička, *Physik der Ferrite und der verwandten magnetischen Oxide* (Academia, Prague, 1973; Mir, Moscow, 1976).

Translated by V. Sakun

$=$ **CONDENSED MATTER** $=$

Computer Simulation of the Crystallization of Amorphous Iron under Isochronous Annealing Conditions

A. V. Evteev*, A. T. Kosilov, and A. V. Milenin

Voronezh State Technical University, Moskovskiĭ pr. 14, Voronezh, 394026 Russia
*e-mail: mfm@ns1.vstu.ac.ru
Received February 8, 2000

Abstract—The isochoric heating of amorphous iron at an average rate of about 6.6×10^{11} K/s was modeled by the molecular dynamics method using the approximation of Pak–Doyama pair potential. The bcc crystallization of the model system was found to occur in the temperature range 1100–1180 K. © *2000 MAIK "Nauka/Inter-periodica".*

PACS numbers: 81.40.Ef; 61.43.Bn

In this work, crystallization in a system of particles with the Pak–Doyama interatomic potential [1] was observed. The empirical Pak–Doyama pair potential has the form of a fourth-order polynomial

$$
\begin{aligned}
\phi(r) = &-0.188917(r - 1.82709)^4 \\
&+ 1.70192(r - 2.50849)^2 - 0.198294 \text{ eV}
\end{aligned}
\tag{1}
$$

(r is expressed in Å). The potential cutoff radius is $r_c =$ 3.44 Å. The parameters of this potential were determined from data on the elastic properties of α-Fe. Its use in the modeling of liquid and amorphous iron provides a good agreement between the calculated and experimental structural properties [2–4].

The molecular dynamics (MD) model was preliminarily applied at $T = 1823$ K to liquid iron with a real density of 7030 kg/m³ [5]. A bcc lattice was used as a starting structure. The model contained 2000 atoms in the basic cube with periodic boundary conditions. At the initial moment, atoms were endowed with velocities according to the Maxwellian distribution. The MD calculation procedure consisted of the numerical integration of equations of motion with time step $\Delta t = 1.523 \times 10^{-15}$ s using the Verlet algorithm in the velocity form [6]. The melting and relaxation of the system were conducted at the indicated temperature for 2000 time steps. Next, the temperature constraint was removed, and thermal equilibrium was attained in the system for 4000 time steps at a constant internal energy (adiabatic conditions). It should be noted that, even though the atoms were initially disposed in the bcc lattice sites, this configuration was highly unstable and almost instantly melted, because the density and temperature of the system corresponded to liquid iron.

The amorphous state was obtained through the instant quenching (using the static relaxation method) of a model melt with density preliminarily increased to 7800 kg/m³ (because of the lack of experimental data, the density was chosen according to the data for α-Fe [7] with a correction of ~1% for amorphization). Next, the system was subjected to isochronous annealing. The corresponding cyclic procedure consisted of a 20-K step elevation of temperature, maintenance of this temperature in the system for 1000 time steps, and the subsequent annealing under adiabatic conditions for 19000 time steps. Thus, the duration of one cycle comprised 20000 time steps or 3.046×10^{-11} s, and the average heating rate was approximately 6.6×10^{11} K/s. After each cycle, the system was transferred to the state with $T = 0$ using the static relaxation method, so that the atoms were allowed to occupy equilibrium positions in the local potential wells.

The following thermodynamic properties were calculated in the course of modeling:

(1) kinetic energy

$$
E_k = \sum_{i=1}^{N} \frac{m v_i^2}{2},
\tag{2}
$$

(2) potential energy

$$
U = \sum_{i=1}^{N-1} \sum_{j=i+1}^{N} \phi(r_{ij}),
\tag{3}
$$

(3) total energy

$$
E = E_k + U,
\tag{4}
$$

(4) and pressure

$$
P = \frac{1}{3V} \left(\sum_{i=1}^{N} m v_i^2 - \sum_{i=1}^{N-1} \sum_{j=i+1}^{N} r_{ij} \frac{\partial \phi(r_{ij})}{\partial r_{ij}} \right),
\tag{5}
$$

where N is the number of atoms, m is the atomic mass, v_i is the velocity of the ith atom, r_{ij} is the distance
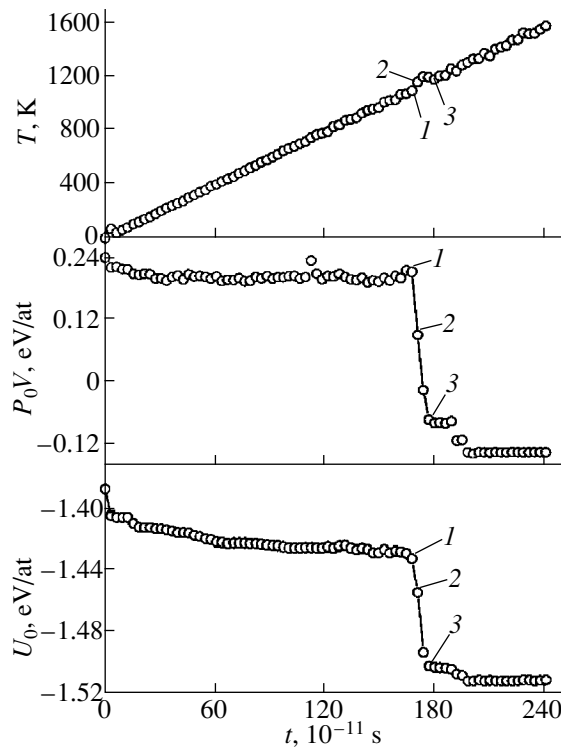
Fig. 1. Time-dependent temperature, product of pressure and volume, and potential energy after static relaxation of the iron model under isochronous annealing conditions. Numbers *1*, *2*, and *3* correspond to times $1100000\,\Delta t$, $1120000\,\Delta t$, and $1180000\,\Delta t$ and to the numbers of plots in Figs. 2 and 3.

between the ith and jth atoms, and V is the volume of the system. The temperature of the system was calculated from the averaged (over the last 16 000 time steps of each cycle) value of kinetic energy

$$T = 2\bar{E}_k/3Nk_B, \qquad (6)$$

where k_B is the Boltzmann constant, and the bar indicates time averaging.

Figure 1 displays the time dependences for the temperature of the model, the product of pressure volume, and the potential energy after the static relaxation of the model. It is seen that a first-order phase transition occurs between the 1100000th and 1160000th time steps ($T \approx 1100$–1180 K). In order to reveal structural changes occurring upon the phase transition, the atomic pair radial distribution functions (APRDF) were calculated and statistical-geometrical analysis based on the Voronoi polyhedra (VP) was carried out, including the calculation of the angular correlation functions (ACF) describing the distribution of angles between the pairs of nearest neighbors and the polyhedron center. The positions of the APRDF (Fig. 2) and ACF (Fig. 3) peaks point to the formation of a crystalline phase with the bcc lattice. The same is confirmed by an analysis of the distribution of VP types. Recall that an individual VP can be described by a set of numbers n_q equal to the number of faces having q sides
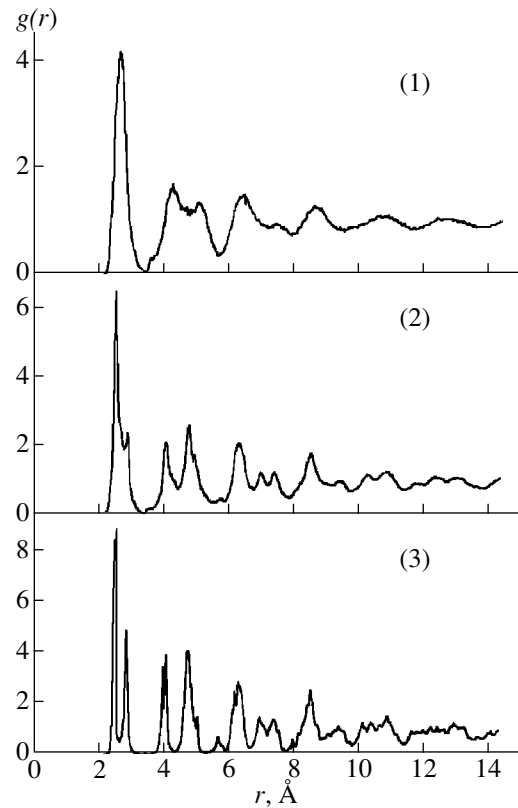

Fig. 2. Atomic pair radial distribution functions $g(r)$ for the statically relaxed models calculated at times (1) $1100000\,\Delta t$, (2) $1120000\,\Delta t$, and (3) $1180000\,\Delta t$.
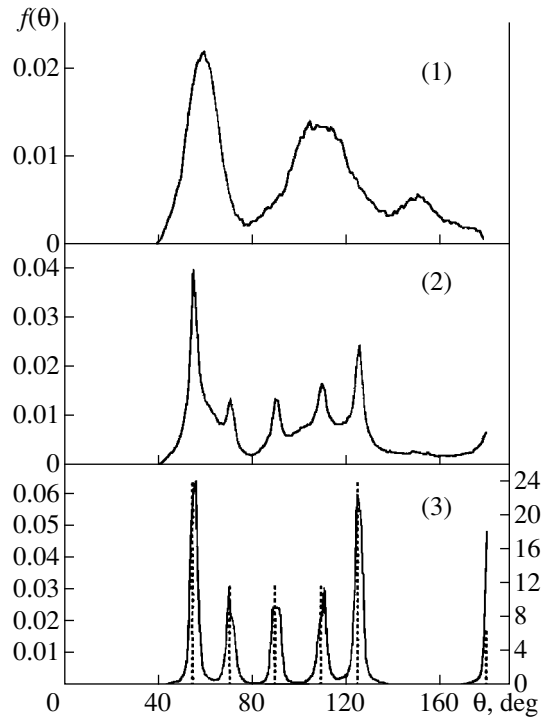

Fig. 3. Angular correlation functions $f(\theta)$ for the statically relaxed models calculated at times (1) $1100000\,\Delta t$, (2) $1120000\,\Delta t$, and (3) $1180000\,\Delta t$. Vertical dotted lines in (3) indicate the angular distribution in a perfect bcc lattice (the right scale).

$(n_3 - n_4 - n_5 - \ldots)$ [8]. After crystallization, the coordination of approximately 90% of the atoms of the model is characterized by the (0-6-0-8) VP (cuboctahedron, Wigner–Seitz cell of the bcc lattice). Further temperature elevation leads to the additional ordering of the crystalline structure, which is completed at $T \approx 1300$ K. In the end, the fraction of atoms characterized by the (0-6-0-8) VP reaches ~97%.

REFERENCES

1. H. M. Pak and M. Doyama, J. Fac. Eng., Univ. Tokyo, Ser. B **30**, 111 (1969).

2. R. Yamamoto, H. Matsuoka, and M. Doyama, Phys. Status Solidi A **45**, 305 (1978).

3. D. K. Belashchenko, Fiz. Met. Metalloved. **60**, 1076 (1985).

4. A. V. Evteev and A. T. Kosilov, Rasplavy **1**, 55 (1998).

5. A. A. Vertman and A. M. Samarin, *Properties of Iron Melts* (Nauka, Moscow, 1969).

6. L. Verlet, Phys. Rev. **159**, 98 (1967).

7. C. J. Smithells, *Metals Reference Book* (Butterworths, London, 1976; Metallurgiya, Moscow, 1980).

8. J. L. Finney, J. Comput. Phys. **32**, 137 (1979).

Translated by A. Bagatur'yants

===== **CONDENSED MATTER** =====

Electrooptical Modulation in the Stark-Ladder Regime[1]

P. Etchegoin

Blackett Laboratory, Imperial College of Science, Technology, and Medicine, SW7 2BZ London, United Kingdom
e-mail: p.etchegoin@ic.ac.uk

Abstract—A direct measurement of the in-plane birefringence below the absorption edge of a GaAs/AlAs superlattice (SL) under electric fields shows a unique type of electrooptical modulation. The SL is sandwiched between two doped AlGaAs alloy layers, which play the simultaneous role of positive (p^+) and negative (n^-) contacts, as well as clad layers, to achieve optical waveguiding. The p–(SL)–n structure is chosen so that, as a function of the externally applied bias, it displays Stark-ladder localization and the quantum confined Stark effect at low and high fields, respectively. We show that this results in an electrooptical modulation, in which the built-in birefringence of the SL initially decreases and shows a crossover to a quadratic increase for larger fields. © 2000 MAIK "Nauka/Interperiodica".

PACS numbers: 78.20.Jq; 42.79.Hp; 71.70.E; 42.25.Lc

Among the diverse electrooptical effects found in bulk semiconductors and microstructures, those based on the modification of the absorption by an applied electric field are most commonly considered for application in amplitude modulators. The light beam is tuned in close resonance with the direct gap absorption which is, on the other hand, modified by the presence of an externally applied electric field. Bearing in mind that moderate changes in absorption may result in drastic amplitude variations of the transmitted/reflected beam, these devices provide an effective approach to modulating the light intensity. A myriad of electrooptical devices based on this principle have been constructed, including vertical [1] and waveguided modulators [2].

Conversely, changes in the linear optical properties *in the transparency region* (below the absorption edge of the structure) upon application of an external electric field are also present. A GaAs/AlAs superlattice (SL) or multiple quantum well (MQW) grown along ($\hat{z} \equiv$ [001]) has the symmetry of the D_{2d} point group and looks isotropic for light propagating with $\mathbf{k}^{\text{light}} \parallel \hat{z}$ and polarization in the $\hat{x}$ ([100])–$\hat{y}$ ([010]) plane. The reduction in symmetry brought about by an electric field $\mathbf{E}$ along $\hat{z}$ permits birefringence, which appears as a phase shift between different polarizations in the plane $\perp$ to $\hat{z}$. From the symmetry point of view, the S_4 and $2C_2'$ axes of D_{2d} are removed by the electric field $\mathbf{E} \parallel \hat{z}$, and the two σ_v planes of the group no longer belong to the same class. Hence, two different optical constants appear for polarizations along $\hat{x}' \equiv (\hat{x} + \hat{y}) \equiv$ [100] and $\hat{y}' \equiv (\hat{x} - \hat{y}) \equiv [1\bar{1}0]$, respectively. A linearly polarized beam, either along $\hat{x}$ or $\hat{y}$, is transformed into elliptically polarized light upon reflection or transmission along $\hat{z}$, on account of the phase-shift difference between $\hat{x}'$- and $\hat{y}'$-polarizations. The magnitude of this phase shift, however, depends on the product of the propagation length (which is usually $\ll 1$ μm along $\hat{z}$) and the field-induced birefringence. Accordingly, only small changes are seen in the conventional geometry of transmission or reflection perpendicular to the surface (a vertical modulator), and sensitive techniques based on acoustooptical modulation are required to observe the in-plane anisotropy produced by $\mathbf{E}$ in the polarization of the light.

A completely different situation takes place for light propagating along the planes (i.e., $\mathbf{k}^{\text{light}} \parallel$ [110]) in a waveguided modulator. In this case, the birefringence has at least two different origins, namely, (i) the boundary conditions for the electric field of the light at the clad layers and (ii) the intrinsic birefringence of the MQWs or SL. The former exists even if the core waveguide material is isotropic and constitutes a classic textbook example of the difference between *transverse electric* and *magnetic* (TE- and TM-) modes in a planar waveguide [3]. The latter, however, is an intrinsic property of the bulk waveguide material based on the anisotropy of the electron bands brought about by the presence of well boundaries. After [4, 5], the effect of the boundary conditions can be minimized if the sample is thick enough (as compared to the wavelength λ of the light), so that the lowest order modes closely resemble the propagation of a free plane wave in the bulk material of the waveguide. In this case, the clad layers greatly improve the efficiency of the transmission along the planes and the coupling to the external light source

---

[1] This article was submitted by the author in English.

through total internal reflection, but the measured optical anisotropy *is an intrinsic property of the bulk material inside the waveguide.*

The application of an external E-field through the doped clad layers results in a modification of the electron bands. Consequent with this change, there is a modulation of the built-in birefringence below the gap for $\mathbf{k}^{light} \perp [110]$, which depends on the modification of dipole-allowed virtual transitions from valence- to conduction-band states for different polarizations [6]. The effect of an external electric field on MQWs and SLs has been extensively studied in the literature [7, 8]. In an isolated QW, the effect of $\mathbf{E} \parallel \hat{z}$ on the confined sub-bands is called the quantum confined Stark effect (QCSE) [9–12]. An isolated confined state of energy E_0 in a QW of thickness d and depth V_b experiences a red shift in energy, which is quadratic in the field for $|\mathbf{E}| < (V_b - E_0)$ (low fields). If $\mathbf{E}$ is further increased, the red shift is $\propto |\mathbf{E}|^\alpha$, with $\alpha < 2$; and for even larger fields the effect is transformed into field-induced tunneling to the continuum states above the barrier. Still another possibility exists if, instead of isolated QWs, we have an SL and minibands for electrons and holes. At low fields, Stark-ladder localization (SLL) occurs and the minibands split into a series of equally spaced states separated by $meEd$ ($m = \pm 1, \pm 2 \dots$ etc.) [8] (with $E \equiv |\mathbf{E}|$). Accordingly, SLL dominates the optical properties close to the absorption edge at low fields. At larger fields, the tunneling process among wells is lessened and the QCSE of isolated excitons in each QW is recovered. SLL can be obtained at room temperature and has been observed several times with optical techniques [13, 14]. Bleuse, Bastard, and Voisin [15] calculated the optical absorption of the Stark ladder in the envelope-function approximation and obtained for SL the important analytic result [15]

$$\alpha(\omega) \sim \sum_{m=-\infty}^{m=+\infty} J_m^2(-\Delta/2eEd)Y(\omega - (\varepsilon + meEd)), \quad (1)$$

where $\Delta = \Delta_c + \Delta_v$ is the total width of the electron and heavy-hole (hh) minibands and $\varepsilon = E_g + E_h + E_e$, with E_g the band gap of the well material and $E_{e,h}$ the confinement energies for electrons and holes, respectively. Equation (1) predicts a blue shift of the absorption edge [15] for increasing (small) E_s. *In the limit where the excitons cannot tunnel to their neighboring wells, the gap of a collection of isolated excitons is half of the total miniband width Δ above the energy of the absorption edge of the SL.* This occurs at fields of the order of $|\mathbf{E}| \sim \Delta/4ed$ [15]. Likewise, once the excitons are isolated in each well, they display the quadratic red shift of the QCSE. In practice, the effect at low fields is less pronounced than the expected blue shift of $\sim\Delta/2$. However, it has been already used for the construction of a modulator which transmits light close to the gap at moderate bias [16]. The blue shift of the absorption edge observed in [16] was smaller than the theoretical

prediction but in qualitative agreement with the predictions of [15]. The existence of SLL implies a certain degree of coherence of the wave functions of the excitons among neighboring wells. This coherence can more easily be lost in samples at room temperature (RT) and with large inhomogeneous broadening, producing the crossover from SLL to the QCSE at even lower fields than those predicted by (1). Summarizing, as the field is increased, we can expect a moderate blue shift of the absorption edge revealing the presence of SLL, followed by a crossover to an inhomogeneously broadened collection of localized excitons characterized by an absorption edge with a red shift as a quadratic function of $\mathbf{E}$.

We now turn to the effect of the field-dependent band structure on the birefringence. It is well known that the dielectric response in the transparency region *close to the absorption edge of a direct gap* can be thought of as coming from a dispersionless contribution of the average (Penn) gap of high-energy transitions, plus a term resonant with the first direct gap [6]. We shall evaluate the optical response in the transparency region at energies which are only ~10% below the gap (ω_{gap}); and, accordingly, the shift of the absorption edge with the applied $\mathbf{E}$ ought to be the leading effect in the modification of the birefringence [17]. We shall show that, in our case, a blue (red) shift of the absorption edge corresponds to a decrease (increase) in the leading resonance term with the direct gap and, thus, to a decrease (increase) in the birefringence $\Delta n(\omega)$ close to the gap (with $\omega < \omega_{gap}$).

In this paper, we measure the birefringence for in-plane propagation of light ($\mathbf{k} \perp \hat{z}$) in a thick superlattice (to minimize waveguiding effects) using the method of transmission through crossed polarizers. The light source is a Ti-Sapphire laser; and the sample must be properly masked to avoid stray light and accommodate, at the same time, the electrical contacts. Further details of the experimental setup and methods were given elsewhere [4, 5]. Measurements are performed on a 300-period GaAs/AlAs SL (3/0.9 nm) sandwiched between n^-- and p^+-Ga$_{0.3}$Al$_{0.7}$As layers doped to 1×10^{18} cm^{-3}, which shows SLL at RT [14]. This sample is entirely equivalent to the one in [14] (where SLL at RT was reported for the first time), except for the fact that our sample has more periods to increase the thickness along $\hat{z}$. As a characterization measurement, we show in Fig. 1 the RT photocurrent spectra at zero bias. Up to six Stark-ladder levels could be observed, in close resemblance with the results of [14]. These peaks spread and outline the characteristic fan chart of SLL for small reverse biases. We shall not dwell on the details of the photocurrent spectra, which are already explained elsewhere [14].

Fig. 2 shows the raw in-plane transmission through crossed polarizers below the gap for a sample with transmission length $l = 1.9$ mm. The data were taken for
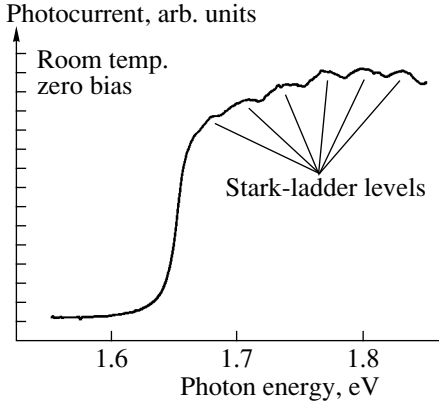
Photocurrent, arb. units

Room temp.
zero bias

Stark-ladder levels

1.6   1.7   1.8
Photon energy, eV

Fig. 1. RT photocurrent spectra at zero bias. See the text for further details.

Transmission, arb. units

69 kV/cm
61
52
44
36
28
20
12

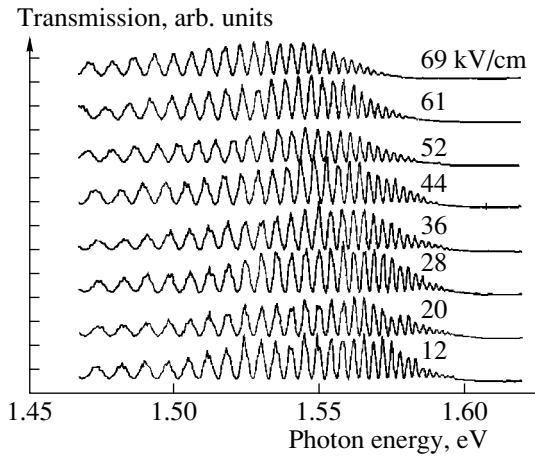1.45   1.50   1.55   1.60
Photon energy, eV

Fig. 2. Raw in-plane transmission data between crossed polarizers for different applied fields. Note the red shift of the extinction point for large fields.

$k^{light} \parallel [110]$ and both incident and output polarizations at 45° with respect to $\hat{z}$. The birefringence oscillations (fringes) in the normalized transmitted intensity are expected to be given by [4, 5]

$$I/I_0 \sim \cos^2[(\pi l/\lambda)\Delta n(\omega)]. \qquad (2)$$

Note that the extinction point, i.e., the energy at which the oscillations vanish, can be seen with the naked eye to red-shift for large fields. The blue shift at low fields is not seen here, because the extinction point is normally a poor measure of small changes in the gap. The number of fringes per unit energy increases as the gap is approached from below, as expected [4, 5] from the resonant behavior of $\Delta n(\omega)$. In Fig. 3, we show a blowup of the fringes in Fig. 2 around ~1.49 eV, together with their percentage energy change. According to (2), each maximum in Fig. 3a is expected to fulfill the condition $l\omega\Delta n(\omega)/2\pi c = M$, where M is a fixed large integer number. For small perturbations of the birefringence, a blue (red) shift in the energy position

of a particular fringe must be compensated by a corresponding decrease (increase) in $\Delta n(\omega)$. Since $M \gg 1$ close to the gap, differences between M and $M + 1$ are negligible and successive maxima show the same percentage energy change as shown in Fig. 3b. Note also that there is a clear crossover between two distinct regions around ~35 kV/cm. We take the energy shifts of specific fringes in Fig. 3a as a clear indication of two different regimes in the electrooptical modulation of $\Delta n(\omega)$ below ω_{gap}, to wit, a blue shift of the gap at small fields followed by a quadratic red shift above ~35 KV/cm. These two regimes correspond to a decrease in the intrinsic $\Delta n(\omega)$ followed by a quadratic increase, respectively.

Very recently [17], we have shown in a systematic study of the in-plane birefringence of MQW's that a good empirical approximation for the $\Delta n(\omega)$ at energies below (but close) to the absorption edge is given by

$$\Delta n(\omega) = \Delta n^0 \frac{\omega_0}{\omega} + \frac{\hbar\Omega}{\hbar\omega}\ln\left[\frac{(\omega_g - \omega_0)\omega}{\omega_0(\omega_g - \omega)}\right], \qquad (3)$$

where ω_g corresponds to the average gap of the SL, Δn^0 is a calibration value at $\omega_0(< \omega_g)$, and $\hbar\Omega$ is an empirically determined parameter of the order of ~0.02 eV (depending on the size of the wells). For small percentage changes, (3) can be linearized and, in this description, the field-induced changes in $\Delta n(\omega)$ should have their counterpart in the position of the average gap. A possible method for the determination of the average gap is to evaluate the mean energy (ω_g) using the luminescence profile (LP) $I(\omega)$ as a weighting factor. This determination is qualitative, for the general shape of $I(\omega)$ depends on the product of the joint density of states and the Boltzmann factor but, nevertheless, should be consistent with the overall picture. Figure 4a displays the LP data at RT for different applied electric fields together with the average gaps calculated as $\omega_g = \int \omega I(\omega)d\omega$. The LP signals are normally faint in our experimental conditions simply because the presence of the mask for the in-plane transmission experiments implies that the data must be excited and collected from the side of the wafer, together with the fact that data are taken at RT and that low excitation powers are used in order to leave the internal bias of the device unaltered. Notwithstanding, it is quite clear that the qualitative behavior of ω_g in Fig. 4b is in excellent agreement with the data in Fig. 3b. The shift of the average gap, together with the description given by (3), produces exactly the sort of modulation in the birefringence seen in Fig. 3a and reveals the microscopic origin of this peculiar electrooptical effect, which shows a crossover between two distinct regimes.

In conclusion, we have shown that a peculiar kind of electrooptical modulation of $\Delta n(\omega)$ in the transparency region ($\omega < \omega_{gap}$) exists in p^+–SL–n^- structures, where SLL is followed by the QCSE. From the total miniband
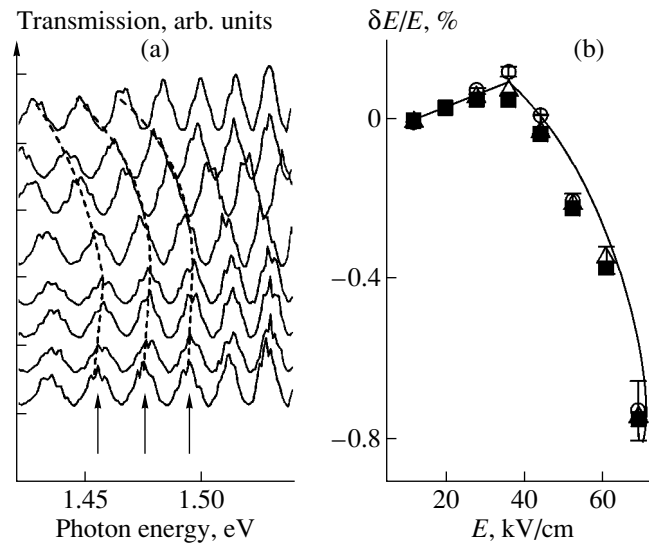
Fig. 3. (a) Birefringence fringes around ~1.49 eV which were continuously followed as a function of the externally applied field. In (b) we show the percentage energy change in the position of three successive fringes. Note a clear crossover between two distinct regimes around ~35 kV/cm. See the text for further details.
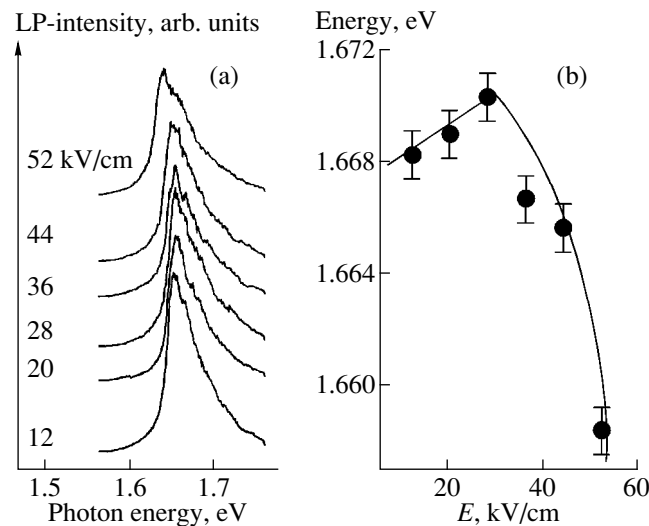

Fig. 4. (a) LP data for different **E**'s. In (b) we show the position of the average gap for different fields, as obtained from the luminescence profiles. A picture consistent with the change in the birefringence fringes of Fig. 3 is obtained.

width of our sample ($\Delta \sim 10$ meV) and the period of the superlattice ($d = 4.1$ nm), the excitons should be completely localized at [15] $E \sim 250$ KV/cm. The crossover occurs, however, at fields which are about six times smaller than the theoretical prediction of [15], which does not take into account disorder (inhomogeneous broadening) and finite temperature. The blue shift of the absorption edge at low fields is also much less than $\Delta/2$ (as observed also in [16]). The qualitative agreement with what is expected for the absorption and its effect on $\Delta n(\omega)$ below the gap are, however, correct. Unlike the conventional Pockels or Kerr electrooptical modulation [3], which are monotonic with the applied field, there is in this case a crossover in both the sign and the field-dependence of the modulation in $\Delta n(\omega)$ as a function of **E**. Peculiar electrooptical applications of this effect could be envisioned.

REFERENCES

1. R. Schwedler, H. Mikkelsen, K. Wolter, *et al.*, J. Phys. III **4**, 2341 (1994).

2. E. Bigan, Doctoral Dissertation (Univ. de Paris-Sud, 1991); S. M. Sze, *Physics of Semiconductor Devices* (Wiley, New York, 1981).

3. A. Yariv, *Optical Electronics* (Saunders College Publ., New York, 1991).

4. A. Fainstein, P. Etchegoin, P. V. Santos, *et al.*, Phys. Rev. B **50**, 11850 (1994).

5. P. Etchegoin, A. Fainstein, A. A. Sirenko, *et al.*, Phys. Rev. B **53**, 13662 (1996).

6. M. Cardona, in *Atomic Structure and Properties of Solids*, Ed. by E. Burstein (Academic, New York, 1972), p. 513.

7. M. Jaros, *Physics and Applications of Semiconductor Microstructures* (Clarendon Press, Oxford, 1989); P. Yu and M. Cardona, *Fundamentals of Semiconductors* (Springer, Berlin, 1995); H. Haug and S. W. Koch, *Quantum Theory of the Optical and Electronic Properties of Semiconductors* (World Scientific, London, 1993).

8. E. E. Méndez, in *Optics of Semiconductor Nanostructures*, Ed. by F. Henneberger, S. Schmitt-Rink, and E. O. Göbel (VCH, Weinheim, 1993).

9. E. J. Austin and M. Jaros, Phys. Rev. B **31**, 5569 (1985).

10. G. Bastard, E. E. Méndez, L. L. Chang, and L. Esaki, Phys. Rev. B **28**, 3241 (1983).

11. D. A. B. Miller, D. S. Chemla, T. C. Damen, *et al.*, Phys. Rev. B **32**, 1043 (1985).

12. D. A. B. Miller, D. S. Chemla, and S. Schmitt-Rink, Phys. Rev. B **33**, 6976 (1986).

13. E. E. Méndez and G. Bastard, Phys. Today **46**, 34 (1993); E. E. Méndez, F. Agulló-Rueda, and J. M. Hong, Phys. Rev. Lett. **60**, 2426 (1988).

14. K. Fujiwara, Jpn. J. Appl. Phys. **28**, L1718 (1989).

15. J. Bleuse, G. Bastard, and P. Voisin, Phys. Rev. Lett. **60**, 220 (1988).

16. E. Bigan, M. Allovon, M. Carre, and P. Voisin, Appl. Phys. Lett. **57**, 327 (1990).

17. A. A. Sirenko, P. Etchegoin, A. Fainstein, *et al.*, Phys. Rev. B **60**, 8253 (1999); Phys. Status Solidi B **215**, 241 (1999).

==== **CONDENSED MATTER** ====

Effect of Domain Boundary on the Electrical Conductivity of a Magnetic Nanocontact

A. K. Zvezdin* and A. F. Popkov**

* Institute of General Physics, Russian Academy of Sciences, ul. Vavilova 38, Moscow, 117942 Russia
** State Scientific Research Institute of Physical Problems, Moscow, 103460 Russia
Received February 8, 2000

Abstract—The conductivity of a magnetic nanocontact with a spin inhomogeneity in the form of a Ginzburg–Bulaevskiǐ domain wall at the center between oppositely magnetized edges is considered. The conductivity of the nanocontact is calculated in the ballistic approximation for Fe, Co, and Ni in the low-temperature limit, with allowance made for the spatial major–minor change in the electron spin energy due to exchange splitting in the edges. The calculations are carried out for the limiting cases of long and short nanocontacts. It is shown that the domain wall formed in a nanocontact causes considerable quantitative and qualitative changes in the dependence of the conductivity on the channel width. © 2000 MAIK "Nauka/Interperiodica".

PACS numbers: 73.61.-r; 75.60.Ch; 75.70.-i

1. The quantum and mesoscopic properties of nanowires and nanocontacts are being intensively studied, both experimentally and theoretically (see [1, 2] and references therein). Magnetic nanocontacts are of particular interest, because, in these contacts, a controlled conductivity variation by an external magnetic field is possible owing to the effect of the giant magnetoresistance. For example, a detailed study of the magnetoresistance of a nanocontact formed by two Ni wires was performed for the cases of their parallel and antiparallel magnetization, and the possibility of a wide variation (by about 200%) of the quantum resistance of such a nanocontact in a relatively weak magnetic field (~100 Oe) was demonstrated [3]. Some micromagnetic properties of Co magnetic point contacts under magnetization reversal in their electrodes were analyzed by numerically solving the micromagnetic equations [4]. The study of the effect of ferromagnetic microbridges formed in antiferromagnetically coupled layers on the hysteretic properties of multilayers [5] is also noteworthy. The theory of magnetoresistance of a wide magnetic contact containing an insulating interlayer was developed by Slonczewski [6]. The electrical properties of a domain wall were studied by Levy and Zhang [7]. A strong effect of domain walls on the conduction properties of Co and Ni magnetic films was observed in experiments [8, 9]. It is well known that in narrow nanocontacts conductivity quantization takes place, and this phenomenon has some specific features in the presence of exchange splitting for the conduction electrons. However, with all these studies, there still is no theory that would adequately describe the conductivity of magnetic nanocontacts.

In this connection, it is of interest to discuss the theory of a narrow magnetic nanocontact that is formed between two highly anisotropic oppositely magnetized edges and contains a domain wall of the "head-to-head" type. In this paper, we consider such a system in the framework of a simplified Ginzburg–Bulaevskiǐ domain-wall DW model, in which the magnetization in the transition region varies in magnitude but the direction of the spin quantization axis remains unchanged [10]. This simplified model allows one to predict the magnetic nanocontact features related to the energy shift for the conduction electron spins that is caused by exchange splitting in the bridge edges. In fact, there is reason to believe that the domain wall formed in a nanodimensional channel belongs to this very type of domain wall.

2. We first consider a long axially symmetric nanocontact that is oriented along the z-axis, has a variable radius $a(z)$, and is characterized by a curvature radius $R = (d^2a(z)/dz^2)^{-1}$ far exceeding the characteristic size δ of the domain wall ($\delta \ll R$). We assume that the magnetization variation between the oppositely magnetized contact edges can be represented in the form $\mathbf{M} = (0, 0, M_z = M\tanh[(x-q)/\delta])$ (δ is the BW width) [10]. In the ballistic limit, the conductivity of the contact is governed by its tunneling properties and determined by the Landauer formula [11]

$$G = \frac{e^2}{h} \sum_{\sigma, n, m} \int_0^\infty \left(-\frac{\partial f_\sigma}{\partial \varepsilon}\right) T_{\sigma, n, m}(\varepsilon)\, d\varepsilon, \qquad (1)$$

where e is the electron charge, h is the Planck constant, $f_\sigma(\varepsilon)$ is the electron energy (ε) distribution function depending on the direction of spin projection σ on the quantization axis z, and $T_{\sigma, n, m}(\varepsilon)$ is the probability of electron transmission through the channel with a given

transverse energy depending on two quantum numbers n and m. In the low-temperature limit $T \longrightarrow 0$, the conductivity of the nanocontact is determined by its transmissivity for the electrons at the Fermi level:

$$G = \frac{e^2}{h} \sum_{\sigma, n, m} T_{\sigma, n, m}|_{\varepsilon = \varepsilon_F}. \qquad (2)$$

The probability of transmission through the nanocontact channel (bridge) containing the domain wall can be found by solving the Schrödinger equation with allowance made for the exchange-splitting energy,

$$-\frac{\hbar^2}{2m}\Delta\psi - J(z)\sigma\psi = \varepsilon\psi, \qquad (3)$$

where $J(z) = J(0)\tanh[(z-q)/\delta]$, with zero boundary conditions for the electron wave function at the lateral boundary of the bridge; i.e., $\psi(|\mathbf{r}| = a(z)) = 0$, where $\mathbf{r}$ is the radius vector in the cylindrical coordinate system. This problem is solved through the factorization of the wave function as $\psi(\mathbf{r}, z) = \Phi(r, \varphi, z)Z(z)$, where the radial part of the $\Phi(r, \varphi, z)$ function satisfies the reduced two-dimensional Schrödinger problem

$$-\frac{\hbar^2}{2m}\Delta_\perp\Phi = \varepsilon_{m, n}\Phi \qquad (4)$$

with the zero boundary condition $\Phi(r = a(z)) = 0$, where

$$\Delta_\perp = \frac{1}{r}\frac{\partial}{\partial r}r\frac{\partial}{\partial r} + \frac{1}{r^2}\frac{\partial^2}{\partial\varphi^2}$$

and φ is the azimuth angle. The solution to this problem is given by the function $\Phi = J_m(\gamma_{m, n}r/a)\exp(i\varphi m)$, where $J_m(x)$ is the Bessel function and $\gamma_{m, n}$ correspond to its zero values; i.e., $J_m(\gamma_{m, n}) = 0$. The eigenvalues of the "transverse" electron energy are determined by the expression $\varepsilon_{m, n} = \gamma_{m, n}^2\hbar^2/2ma^2$. In the limiting case of a long nanocontact $R \gg \delta$, one can neglect the weak dependence of both the transverse energy $\varepsilon_{m, n}(z)$ and the radial part of the wave function $\Phi(r_\perp, z)$ on the z-coordinate (adiabatic approximation). Then, the remaining part of the wave function $Z(z)$ satisfies the one-dimensional Schrödinger problem of transmission through a potential barrier,

$$-\frac{\hbar^2}{2m}\frac{d^2Z}{dz^2} - J(z)\sigma Z = (\varepsilon - \varepsilon_{m, n})Z, \qquad (5)$$

where $J(z) = J_0\tanh[(z-q)/\delta]$ and $\sigma = \pm 1$. This problem can be solved exactly (see e.g., [12]). In the latter equation, the terms $\sim\Phi^{-1}(d^2\Phi/dr^2)(da(z)/dz)^2$, $(d\ln\Phi/dr)^2(d^2a(z)/dz^2)$ are omitted. Evidently, this approximation is valid when $k_F^2 aR$ and $(k_F R)^2 \gg 1$ at the Fermi level. If one assumes that the asymptotics of the wave function $Z(z)$ away from the barrier at $z \longrightarrow -\infty$ has the form $Z(z) = C_1[\exp(ik_{n, m}z) + A_r\exp(-ikz)]$,

where A_r is the relative amplitude of the reflection wave and $k = [(2m/\hbar^2)(\varepsilon - \varepsilon_{m, n} - \sigma J_0)]^{1/2}$ is the wave number of the incident wave, then the complete solution to the problem (see [12]) is determined by the hypergeometric function

$$Z(z) = \exp(ik'_{n, m}z)F(i\delta(k_{n, m} - k'_{n, m})/2,$$
$$-i\delta(k_{n, m} + k'_{n, m})/2, -i\delta k'_{n, m} + 1, -\exp(-2z/\delta)),$$

where $k'^2_{n, m} = (2m/\hbar^2)(\varepsilon - \varepsilon_{m, n} + \sigma J_0)$. In this case, the transmissivity $T = 1 - |A_r|^2$ is equal to

$$T_{n, m} = 1 - \frac{\sinh^2[\pi(\delta/2)(k_{n, m} - k'_{n, m})]}{\sinh^2[\pi(\delta/2)(k_{n, m} + k'_{n, m})]}, \qquad (6)$$

Taking into account that the summation over the energies with allowance made for the equivalence of the overbarrier reflection coefficients yields the same result for the major and minor electrons and using the expression derived from the Landauer formula (2), one obtains for zero temperature in the long-wave-length limit $k\delta \ll 1$

$$G_{\uparrow\downarrow} = \frac{2e^2}{h}\sum_{n, m}\frac{4k_{n, m}k'_{n, m}}{(k_{n, m} + k'_{n, m})^{1/2}}\Bigg|_{\varepsilon = \varepsilon_F}\theta(\varepsilon_F - J_0 - \varepsilon_{m, n}), (7)$$

where $\theta(x)$ is the Heaviside function. In the absence of the domain boundary, the transmissivity of the channel for the electrons above the Fermi level is equal to unity and, therefore,

$$G_{\uparrow\uparrow} = \frac{e^2}{h}\sum_{n, m}[\theta(\varepsilon_F - J_0 - \varepsilon_{m, n}) + \theta(\varepsilon_F + J_0 - \varepsilon_{m, n})]. (8)$$

It follows from this formula that the difference in the Fermi level shifts for the major and minor electrons leads to the splitting of the conductivity steps that appear in the cylindrical contact upon variation of the bridge radius. For the antiparallel magnetization of the edges, this splitting is absent.

The calculated contact conductivity $G(k_F a)$ is shown in Fig. 1 (in $2e^2/h$ units) as a function of the normalized channel radius $k_F a$, where k_F is the wave number at the Fermi level. The calculations were performed for iron with the use of the formulas derived above for the parallel and antiparallel magnetizations of the contact edges (curves 1 and 2, respectively). It follows from these calculations that, first, the curve for the conductivity vs. normalized channel width $k_F a$ is shifted in such a way that the conductivity of a contact containing the domain wall decreases. Second, the shape of the $G(k_F a)$ curve between the conductivity jumps also changes: in the presence of the domain wall in the channel, the conductivity steps are smoothed out.

Figure 2 presents the changes $\Delta G(k_F a) = G_{\uparrow\uparrow} - G_{\uparrow\downarrow}$ occurring in the channel conductivity upon the forma-
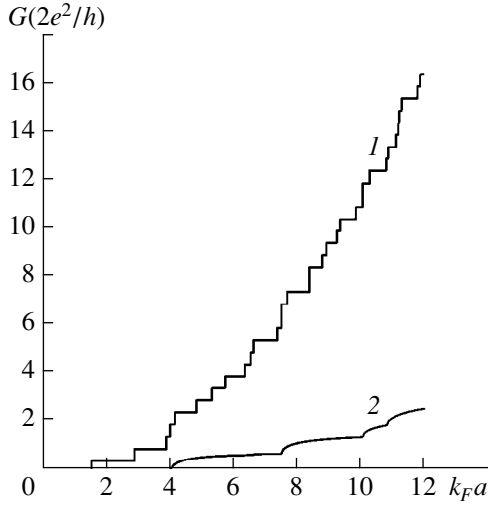
Fig. 1. Dependence of the conductivity of a long cylindrical channel on its normalized width for the Fe nanocontact: (*1*) in the absence of the domain wall in the channel and (*2*) for the antiparallel spin orientations in the edges.
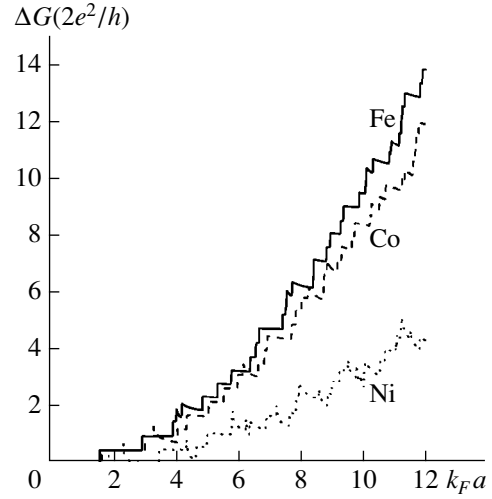

Fig. 2. Change in the conductivity of a long nanocontact caused by the repolarization of its edges and appearance of a domain wall inside the channel: solid curve is for Fe, dashed curve is for Co, and dotted curve is for Ni.

tion of a domain wall of the "head-to-head" type inside the channel. The calculations were performed for Fe, Co, and Ni with allowance made for the transverse quantization of the electron states. The parameter $J_0/\varepsilon_F = \nu$ was taken equal to $\nu = 0.74$, 0.61, and 0.217, respectively (according to [6]). For the case under study, the expected variation in the magnetoresistance proved to be much higher than that predicted by the analogous theory for boundless contacts containing an insulating interlayer [6]. This is due to the fact that the insulating interlayer strongly reduces the effect of magnetization on the contact conductivity.

3. We now consider a contact with a high curvature of the bridge between the edges; i.e., $\delta \gg R$. In this case, one can expect that the spatial variation of the "transverse energy" $\varepsilon_{m,n} = \gamma_{m,n}^2 \hbar^2/2ma^2(z)$ (will play the governing role and the potential gradient produced by the domain wall will shift the maximum of the effective potential barrier and change its height. Indeed, for the aforementioned second Schrödinger problem, which determines the probability of electron transmission, the total potential can be reduced to the following form:

$$U(z) = \gamma_{m,n}^2 \hbar^2/2ma^2(z) - \sigma J(z) \approx (\gamma_{m,n}^2 \hbar^2/2ma^2)$$
$$\times (1 - z^2/R^2) + \sigma J_0 \tanh[(z-q)/\delta]$$
$$\approx \varepsilon_{n,m}^0 - \gamma_{m,n}^2 \hbar^2/2ma^2((z - \sigma z_0)/R)^2,$$

where $\varepsilon_{n,m}^0 = \gamma_{m,n}^2 \hbar^2/2ma^2 - \sigma J_0 q/\delta + (J_0^2 ma^2/2\gamma_{m,n}^2 \hbar^2)R^2/\delta^2$ and $z_0 = (J_0 ma^2/\gamma_{m,n}^2 \hbar^2)R^2/\delta$. By solving the Schrödinger problem with allowance made for the barrier, one arrives at the following formula for

the electron transmissivity at the Fermi level $\varepsilon_F = \hbar^2 k_F^2/2m$:

$$T_{n,m} = \frac{1}{1 + \exp(-Q_{m,n})}, \qquad (9)$$

$$Q_{m,n} = Q_{m,n}^{(0)} + Q_{m,n}^{(1)} + \sigma Q_{m,n}^{(2)},$$

$$Q_{m,n}^{(0)} = (\pi R a k_F^2/\gamma_{m,n})[1 - (\gamma_{m,n}/ak_F)^2],$$

$$Q_{m,n}^{(1)} = (\pi R k_F)(J_0/\varepsilon_F)^2 (ak_F/\gamma_{m,n})^3 R^2/\delta^2,$$

$$Q_{m,n}^{(2)} = (\pi R k_F)(J_0/\varepsilon_F)(ak_F/\gamma_{m,n})q/\delta.$$

From the Landauer formula, one then obtains

$$G_{\uparrow\downarrow} = \frac{e^2}{h} \sum_{\sigma, n, m} \frac{1}{1 + \exp(Q_{n,m})} \theta(\varepsilon_F - J_0 - \varepsilon_{m,n}). \quad (10)$$

In the short-wavelength limit $Rk_F \gg 1$, formula (10) can be approximated by the expression

$$G_{\uparrow\downarrow} = G_0 + \left\langle \left(\frac{\partial G}{\partial Q}\right)_0 Q^{(1)} \right\rangle + \left\langle \left(\frac{\partial G}{\partial Q}\right)_0 Q^{(2)} \right\rangle$$
$$+ \frac{1}{2}\left\langle \left(\frac{\partial^2 G}{\partial Q^2}\right)_0 Q^{(2)} \right\rangle^2 + \ldots \approx G_0 + \left\langle \left(\frac{\partial G}{\partial Q}\right)_0 Q^{(1)} \right\rangle \quad (11)$$
$$+ \frac{1}{2}\left\langle \left(\frac{\partial^2 G}{\partial Q^2}\right)_0 Q^{(2)} \right\rangle^2.$$

One can see from this formula that the presence of a domain wall in a short contact results in two effects. First, the jumps in the resistance vs. normalized bridge width curve are nonuniformly shifted proportionally to

the $\Delta_1(ak_F) \sim (J_0/\varepsilon_F)^2(ak_F/\gamma_{m,n})^3R^2/\delta^2$ factor. Second, the displacement of the center of the domain wall also non-uniformly shifts the jump positions proportionally to the factor $\Delta_2(ak_F) \sim (J_0/\varepsilon_F)(ak_F/\gamma_{m,n})q/\delta$. The latter effect can be controlled by the external magnetic field, owing to the dependence of the DW displacement on the magnetic field $q(H)$.

ACKNOWLEDGMENTS

REFERENCES

1. J. L. Costa-Krämer, N. García, P. García-Mochales, *et al.*, Phys. Rev. B **55**, 5416 (1997).

2. E. N. Bogachek, M. Jonson, R. I. Shekhter, and T. Swahn, Phys. Rev. B **50**, 18341 (1994).

3. N. García, M. Munoz, and Y.-W. Zhao, Phys. Rev. Lett. **82**, 2923 (1999).

4. R. P. van Gorkom, S. J. C. H. Theeuwen, K. P. Wellock, *et al.*, J. Appl. Phys. (1999) (in press).

5. J. F. Bobo, H. Kikuchi, O. Redon, *et al.*, Phys. Rev. B **60**, 4131 (1999).

6. J. C. Slonczewski, Phys. Rev. B **39**, 6995 (1989).

7. P. M. Levy and S. Zhang, Phys. Rev. Lett. **79**, 5111 (1977).

8. M. Viret, D. Vignoles, D. Cole, *et al.*, Phys. Rev. B **53**, 8464 (1996).

9. J. F. Gregg, W. Allen, K. Ounadjela, *et al.*, Phys. Rev. Lett. **77**, 1580 (1996).

10. L. N. Bulaevskiĭ and V. L. Ginzburg, Pis'ma Zh. Éksp. Teor. Fiz. **11**, 272 (1970) [JETP Lett. **11** (1970)].

11. R. Landauer, IBM J. Res. Dev. **1**, 223 (1957).

12. L. D. Landau and E. M. Lifshitz, *Quantum Mechanics: Non-Relativistic Theory* (Nauka, Moscow, 1989, 4th ed.; Pergamon, Oxford, 1977, 3rd ed.).

Translated by E. Golyamina

=========================== **MISCELLANEOUS** ===========================

Relative Diffusion Transform and Quantum Speedup of Computations[1]

Yu. I. Ozhigov* and N. B. Victorova**

* Department of Applied Mathematics, Moscow State Technological University "Stankin", Moscow, 101472 Russia
e-mail: y@oz.msk.ru
** Department of Differential Equations and Functional Analysis, Russian University of Peoples' Friendship,
ul. Miklukho-Maklaya 6, Moscow, 117198 Russia

Received January 26, 2000

Abstract—It is shown that every function computable in time $T(n)$ and space $S(n)$ on a classical one-dimensional cellular automaton can be computed with certainty in time $O(T^{1/2}S)$ and space $n\sqrt{T}$ on a quantum computer with relative diffusion transforms (RDTs) on parts of intermediate products of classical computation. However, in the general case, RDTs cannot be implemented by the conventional quantum computer even with oracles for intermediate results. Such a function can be computed only in time $O(S4^{S/2}T/T_1)$ on the conventional quantum computer with oracles for the intermediate results of classical computations with time T_1. © 2000 MAIK "Nauka/Interperiodica".

PACS numbers: 03.67.Lx

Quantum mechanical computations are different in nature from the classical ones (see [1–3]). One of the most intriguing features of quantum computers is their ability to speed up searching. L. Grover [4] constructed a quantum algorithm that for a given function $F: \{0, 1\}^n \longrightarrow \{0, 1\}$ finds the unique solution of the equation $F(x) = 1$ after $O(\sqrt{N})$ quantum evaluations of F, whereas every classical computer requires $\Omega(N)$ evaluations, $N = 2^n$.

With Grover's algorithm for a search as a good precedent, it is of interest to elucidate whether it is possible to speed up the complicated classical algorithms on quantum computers, transforming classical programs into quantum ones. Most likely, this cannot be done without some additional information on the classical algorithm. Such information in its simplest form is an oracle testing intermediate results. Let the work of a classical algorithm on an input word A have the form $x_0(A) \longrightarrow x_1(A) \longrightarrow \dots \longrightarrow x_T(A)$. Given $T_1 < T$, the intermediate result is the $\{\langle A, x_{T_1}(A) \rangle$ set. An oracle for this set is called the verifier.

The following Theorem 1 shows that verifier can speed up only sufficiently long computations. Theorem 2 exhibits the potentials of the relative diffusion transform (RDT).

Theorem 1. *Every function $F: \omega^* \longrightarrow \omega^*$ (card(ω) = 4), computable on a classical one-dimensional cellular automaton with alphabet ω in time $T(n)$ and space $S(n)$ can be computed in time $T_q = O(S4^{S/2}T/T_1)$ and space S on a quantum computer with*

a verifier for the intermediate results of F corresponding to time T_1.

Theorem 2. *Every function $F(n)$ computable in time $T(n)$ and space $S(n)$ on a classical one-dimensional cellular automaton can be computed in time and space $O(T^{1/2}S)$ on a quantum computer with RDT on parts of intermediate results of F corresponding to time $T_1 = T^{1/2}S$.*

Note that, in the general case, RDT cannot be localized (e.g., represented as a tensor product of small matrices) and cannot be replaced by the computations on a quantum query machine (see [5] for the definition) of polynomial time complexity. Therefore, generally speaking, the speedup by Theorem 2 cannot be achieved on a quantum query machine.

Quantum computations. We shall use a simple model of a quantum computer with two parts: the classical part, which transforms by classical laws (say, as a cellular automaton), and the quantum part, which transforms by quantum mechanical principles.

Quantum part. It is an $\mathcal{E} = \{v_1, v_2, \dots, v_r\}$ (r even) set whose elements are called qubits. Each qubit takes values from the $\{z_0\mathbf{0} + z_1\mathbf{1} | z_1, z_2 \in C, |z_0|^2 + |z_1|^2 = 1\}$ set. Here, $\mathbf{0}$ and $\mathbf{1}$ are referred to as the basic states of a qubit. They form a basis of C^2. It is convenient to divide $\mathcal{E}$ into registers of two neighboring qubits, so that any register takes values from $\omega = \{0, 1, 2, 3\}$.

The basic state of the quantum part is a function of the form $e: \mathcal{E} \longrightarrow \{0, 1\}$. The e state can be encoded as $|e(v_1), e(v_2), \dots, e(v_r)\rangle$ and naturally identified with the corresponding word in alphabet ω.

---

[1] This article was submitted by the authors in English.

Let $e_0, e_1, \ldots, e_{K-1}$ all be basic states taken in some fixed order and $\mathcal{H}$ be a K-dimensional Hilbert space with orthonormal basis $e_0, e_1, \ldots, e_{K-1}$, $2^r = K$. This Hilbert space can be regarded as a tensor product $\mathcal{H}_1 \otimes \mathcal{H}_2 \otimes \ldots \otimes \mathcal{H}_r$ of two-dimensional spaces, where $\mathcal{H}_i$ is generated by the possible values of $e(v_i)$, $\mathcal{H}_i \cong C^2$. The (pure) state of the quantum part is an element $x \in \mathcal{H}$ such that $|x| = 1$. Thus, contrary to the classical devices, the quantum device may not only be in the basic state, but also in a coherent state, and this imparts surprising properties to such devices.

Let $\mathcal{H} = \{0, 1, \ldots, K-1\}$. For elements $x = \sum_{s \in \mathcal{H}} \lambda_s e_s$, $y = \sum_{s \in \mathcal{H}} \mu_s e_s \in \mathcal{H}$, their dot product $\sum_{s \in \mathcal{H}} \lambda_s \bar{\mu}_s$ is denoted by $\langle x|y \rangle$, where $\bar{\mu}$ means complex conjugation of $\mu \in C$; hence $\langle x|y \rangle = \overline{\langle y|x \rangle}$.

Unitary transformations. Let $\{1, \ldots, r\} = \bigcup_{i=1}^l L_i^s$, $L_i^s \cap L_j^s = \varnothing$ ($i \neq j$), and unitary transformation U_i^s act on $\bigotimes_{j \in L_i^s} e_j$; then $U^s = \bigotimes_{i=1}^l U_i^s$ acts on $\mathcal{H}$, $s = 1, 2, \ldots, M$. We require that all U_i^s belong to a certain finite set of transformations that are independent of $\mathcal{E}$ and can be easily accomplished by physical devices.

Computation is a sequence of unitary transformations $U^1, U^2, \ldots, U^M$. It is applied to some initial state χ_0.

Classical part of the computer points to partitions $\bigcup L_i$ and chooses transformations U_i^s sequentially for each s.

Observations. Let $\chi = \sum_{s \in \mathcal{H}} \lambda_s e_s$ be some fixed state of the computer, often $\chi = \chi_M$. If $A \in \{0, 1\}^k$ is a list of possible values for the first k qubits, then we put

$$B_A = \{i| \exists a_{k+1}, a_{k+2}, \ldots, a_r \in \{0, 1\}:$$

$$e_i = A a_{k+1} a_{k+2} \ldots a_r\}.$$

This observation results in a new state $\chi^A = \sum_{i \in B_A} \dfrac{\lambda_i}{\sqrt{p_a}} e_i$,

where $p_A = \sum_{i \in B_A} \lambda_i^2$.

The observation of the first register in state χ is a procedure which gives a $<$ classical word A, quantum state $\chi^A >$ pair with probability p_A for any possible $A \in \{0, 1\}^k$. The only way to learn the results of quantum computations is to obtain such words A.

Diffusion transform. Every unitary transformation $U: \mathcal{H} \longrightarrow \mathcal{H}$ can be represented by its matrix $U = (u_{ij})$, where $u_{ij} = \langle U(e_j)|e_i \rangle$, so that for $x = \sum \lambda_p e_p$ and $U(x) = \sum \lambda'_p e_p$ we have $\bar{\lambda}' = U\bar{\lambda}$, where $\bar{\lambda}, \bar{\lambda}'$ are columns.

The diffusion transform D is defined by its matrix D: $d_{ij} = 2/N$ if $i \neq j$, and $d_{ij} = -1 + 2/N$ if $i = j$. Note that $D = WRW$, where R is the phase inversion of e_0 and W is the Walsh–Hadamard transform defined as the tensor product of n matrices

$$\begin{pmatrix} 1/\sqrt{2} & 1/\sqrt{2} \\ 1/\sqrt{2} & -1/\sqrt{2} \end{pmatrix},$$

hence, the diffusion transform can be performed on a quantum computer.

For any state $x = \sum_{p \in \mathcal{H}} \lambda_p e$, the average amplitude is taken as $x_{av} = \sum_{p \in \mathcal{H}} \lambda_p/N$. Hereafter, $\mathcal{H}$ denotes the real Euclidean space.

Proposition 1 [4]. *For every state x $\langle e_p|x \rangle - x_{av} = x_{av} - \langle e_p|D(x) \rangle$.*

This means that D is the inversion about the average. We need to relate this property to a subspace $\mathcal{H}_0 \subseteq \mathcal{H}$. Let $\mathcal{H}_0$ be a subspace of $\mathcal{H}$ with basis $e_0, \ldots, e_{M-1}$. Define the relative diffusion transform $D^{\mathcal{H}_0}$ by

$$d_{ij}^{\mathcal{H}_0} = \begin{cases} 2/M & \text{if} \quad i \neq j; \ i, j \in \mathcal{H}, \\ -1 + 2/M, & \text{if} \quad i = j \in \{0, \ldots, M-1\}, \\ \delta_{ij}, & \text{in other cases.} \end{cases}$$

Given state $x = \sum_{p=0}^{M-1} \lambda_p e_p$, its average amplitude is taken as $x_{av}^{\mathcal{H}_0} = \sum_{p=0}^{M-1} \lambda_p/M$. Proposition 1 can easily be extended to the RDTs as follows.

Proposition 2. *For every $p = 0, 1, \ldots, M-1$ $\lambda_p - x_{av}^{\mathcal{H}_0}$* $= x_{av}^{\mathcal{H}_0} - \langle e_p|D^{\mathcal{H}_0}(x) \rangle.$

The diffusion transforms and a simple transformation changing the sign of the target state were sequentially applied in [4] for the fast quantum search. Any iteration increases the amplitude of the target state (initially taken as $1/\sqrt{N}$) by approximately $1/\sqrt{N}$. Therefore, Grover's algorithm requires $O(\sqrt{N})$ steps for the target state to be really observable.

Q–M **speedup.** Suppose that we have a function F: $\omega^* \longrightarrow \omega^*$ computable in time $T(n) > n^2$ and space $S(n) = n$ on a classical Turing machine or cellular automaton. Our goal is to compute F faster than $\Omega(T(n))$ on a quantum computer with RDTs.

Let f: $\omega^* \longrightarrow \omega^*$ denote one step of the classical algorithm for computing F. If F is a one-dimensional cellular automaton with radius R, the neighborhood of radius R of each ith letter in $\bar{a}$ determines the ith letter in $f(\bar{a})$. Without loss of generality, we can assume that $card(\omega) = 4$, because every cellular automaton can be

simulated without slowdown by such a cellular automaton with an appropriate radius. Define for every $a \in \omega^*$ $f^{(0)}(a) = a$, so that $f^{(m)}(a) = f(f^{(m-1)}(a))$ is the mth iteration of f, $f^{(C)} = F$.

Proof of Theorem 1. We can assume that $T > n4^{n/2}$, because otherwise $T = O(T_q)$. Prepare the state $\frac{1}{4^{n/2}}\sum_x |x\rangle$. Now, using an oracle and applying Grover's algorithm, we obtain $f^{(T_1)}(x_0)$ in time $4^{n/2}n$. Then iterate this procedure and obtain sequentially $f^{(2T_1)}(x_0)$, $f^{(3T_1)}(x_0), \ldots, f^{(T)}(x_0)$, which requires the time T_q. Theorem 1 is proved.

Proof of Theorem 2. Fix integers n, T_1, T_2: $T_1 T_2 = T(n)$. Let T_1 independent processors be given: P_1, P_2, …, P_{T_1}, every P_i having the quantum part $B_i = \{1, 2, \ldots, 3n\}$. The pure states for all P_i will have the form $|a_1, \ldots, a_{3n}\rangle$, where all $a_i \in \omega$.

Let us first prepare the state $\frac{1}{k^{n/2}}\sum_{\bar{a}} |\bar{0}, \bar{a}, \bar{0}\rangle$ in each processor by applying the Walsh–Hadamard transformation to all states of the form $|\bar{0}, 0, \ldots, 0, a, 0, \ldots, 0, \bar{0}\rangle$, $\bar{a} = (a_{i_1}, \ldots, a_{i_n})$, where $\bar{0} = 0^n$, $\bar{a} = (a_{i_1}, \ldots, a_{i_n})$. Then calculate the T_2-iteration of f in the last registers to obtain the state $X_0 = \frac{1}{k^{n/2}}\sum_{\bar{a}} |\bar{0}, \bar{a}, f^{(T_2)}(\bar{a})\rangle$ in all processors. This takes $O(T_2)$ steps. Then denote the state $|f^{(iT_2)}(x_0), \bar{a}, f^{(T_2)}(\bar{a})\rangle$ by $\xi_i(\bar{a})$.

Then, the processors work in a serial mode to compute sequentially the intermediate results tar_1, tar_2, …, tar_{T_1}, where $\text{tar}_i = \frac{1}{k^{n/2}}\sum_{\bar{a}} \xi_i(\bar{a})$, x_0 is a certain fixed input word of length n.

Beginning with tar_i, the processor P_i achieves the pure state

$$\text{tar}^*_{i+1} = |f^{(iT_2)}(x_0), f^{(iT_2)}(x_0), f^{(iT_2+T_2)}(x_0)\rangle$$

in time $O(n^2)$. Then the state tar_{i+1} is prepared for the successive processor P_{i+1} that is initially set to the state X_0. The last passage is quite clear; it takes an instant, so that we only need to describe the first passage $\text{tar}_i \longrightarrow \text{tar}^*_{i+1}$.

Omitting indices, denote our target state by tar*. Let $\mathcal{H}_0$ be the Euclidean space with orthonormal basis $\mathcal{B}_0$ consisting of all vectors of the form $\xi_i(\bar{a})$. We have tar* $= |\alpha_1, \ldots, \alpha_n, \alpha_1, \ldots, \alpha_n, \beta_1, \ldots, \beta_n\rangle$. $\mathcal{B}_s$ denotes the set of all vectors of the form $|\alpha_1, \ldots, \alpha_n, \alpha_1, \ldots, \alpha_s, \gamma_{s+1}, \ldots, \gamma_{2n-s}\rangle$ from $\mathcal{B}_0$, $s = 0, \ldots, n$.

Define $\mathcal{H}_s$ as the subspace of $\mathcal{H}_0$ spanned by all vectors from $\mathcal{B}_s$. Then,

$$\dim \mathcal{H}_s = k^{n-s},$$

$$\{\text{tar}\} = \mathcal{H}_n \subset \mathcal{H}_{n-1} \subset \ldots \subset \mathcal{H}_1 \subset \mathcal{H}_0.$$

Now apply the following procedure sequentially for $j = 1, 2, \ldots, n$, beginning with tar. (a) Rotation of all $\xi \in \mathcal{B}_j$. (b) Ensuring RDT $D^{\mathcal{H}_{j-1}}$.

Finally, let us observe the quantum part. If $k = 4$, then at the instant of observation "tar*" has amplitude 1. To show this, the following lemma is required. Let χ_j be the result of the jth step of our procedure (a), (b), $\chi_0 = $ tar.

Lemma 1. *For all $\xi \in \mathcal{B}_j$, $j = 0, 1, \ldots, n$ $\langle \chi_j | \xi \rangle = (3 - 4/k)^j / k^{n/2}$.*

Sketch of the proof. Induction on j. Basis follows from the choice of χ_0. Step follows from Proposition 2. Now put k = 4; Lemma 1 yields $\langle \chi_j | \xi \rangle = 2^j / k^{n/2}$. Consequently, $\langle \chi_n | \text{tar}^* \rangle = 1$.

This computation of F requires the time $O(T^{1/2}n)$ if we put $T_1 = O(T^{1/2}n)$. Lemma 1 is proved. Theorem 2 is proved.

Power of RDT.

Theorem 3. *1) RDTs cannot be implemented on a quantum query machine in polynomial time.*

2) Any device capable of performing RDTs on the sets localized by arbitrary oracles can find the solution of equation $f(x) = 1$ for a given oracle f in polynomial time with a high probability, provided that this solution is unique.

Proof of Theorem 3.

Lemma 2. *Let f be a one-to-one function $\omega^n \longrightarrow \omega^n$,*

$$k = \text{card}(\omega) = 4,$$

$$x_0(f) = \frac{1}{k^{n/2}}\sum_{\bar{b}} |f(\bar{b}), \bar{b}\rangle, \quad \bar{a} \in \omega.$$

Then the value $f(\bar{a})$ can be found with certainty in time $O(n^2)$ on a computer with RDTs on all sets of the form

$$N_{\varepsilon_1 \ldots \varepsilon_k}$$

$$= \{\langle f(\bar{a}), \bar{a}\rangle \mid \exists \varepsilon_{k+1}, \ldots, \varepsilon_n : \bar{a} = \varepsilon_1 \ldots \varepsilon_k \varepsilon_{k+1} \ldots \varepsilon_n\}.$$

Proof. Let $\mathcal{B}_j$ be a set of vectors of the form $|f(\bar{b}), \bar{b}\rangle$, such that the first j components of $\bar{a}$ and $\bar{b}$ are equal, and $\mathcal{H}_j$ be the Euclidean space with the basis $\mathcal{B}_j$.

Then $\{|f(\bar{a}), \bar{a}\rangle\} = \mathcal{H}_n \subset \mathcal{H}_{n-1} \subset \ldots \subset \mathcal{H}_0$. Apply rotation of all $\xi \in \mathcal{B}_j$ and RDT $D^{\mathcal{H}_{j-1}}$ sequentially for $j = 1, 2, \ldots, n$. This yields $|f(\bar{a}), \bar{a}\rangle$ by Lemma 1. Lemma 2 is proved.

(1) Consider the computation with RDTs from Lemma 2, depending on f: $x_0(f) \longrightarrow x_1(f) \longrightarrow \ldots \longrightarrow x_p(f)$, $p = O(n^2)$.

Consider some other function $\tilde{f}$ that differs from f only in two arguments, including $\bar{a}$. Then $\|x_0(\tilde{f}) - x_0(f)\| \le 2/\sqrt{N}$, $N = 4^n$. Assume that RDTs can be implemented in polynomial time with the corresponding oracles for $N_{e_1 \ldots e_k}$. By the definition of $\tilde{f}$, the corresponding postquery states x_m $m = 1, 2, \ldots, p$ for the computations of $f(\bar{a})$ and $\tilde{f}(\bar{a})$ differ by $mP(n)/\sqrt{N}$, where $P(n)$ is a polynomial, as is shown in [5]. But it is impossible, because for the final pure states $x_p(f) = |\bar{a}, f(\bar{a})\rangle$, $x_p(\tilde{f}) = |\bar{a}, \tilde{f}(\bar{a})\rangle$, we have $\|x_p(f) - x_p(\tilde{f})\| = \sqrt{2}$. Point 1) is proved.

(2) Consider an oracle for f and find a solution of equation $f(x) = 1$ with RDTs. Put $\mathcal{B}_m = \{\langle x, y \rangle | y = f(x) \& (y = 1 \vee \exists x': x = (0, 0)^m x'\}$ $(0, 0) \in \omega$. Then we have: $|\mathrm{card}(\mathcal{B}_m) - 4^{n-m}| \le 1$, because the solution is unique. Therefore, applying the algorithm from the proof of Lemma 2, we obtain the desired $|\mathrm{card}(\mathcal{B}_m) - 4^{n-m}| \le 1$ with high probability in time $O(n^2)$. Theorem 3 is proved.

REFERENCES

1. A. Barenco and A. Ekert, Acta Phys. Slov. **45**, 1 (1993).
2. S. Lloyd, Science (Washington, D.C.) **261**, 1569 (1993).
3. A. Steane, http://xxx.lanl.gov/archive/quant-ph/9708022.
4. L. K. Grover, http://xxx.lanl.gov/archive/quant-ph/9605043.
5. C. H. Bennett, E. Bernstein, G. Brassard, and U. Vazirani, SIAM J. Comput. (in press); http://xxx.lanl.gov/archive/quant-ph/9701001.